Computational Systems Mechanobiology of Tumor-Induced Angiogenesis

by

Amirmahdi Mostofinejad

A thesis
presented to the University of Waterloo
in fulfillment of the
thesis requirement for the degree of
Master of Applied Science
in
Civil Engineering

Waterloo, Ontario, Canada, 2019

Author's Declaration

I hereby declare that I am the sole author of this thesis. This is a true copy of the thesis, including any required final revisions, as accepted by my examiners.

I understand that my thesis may be made electronically available to the public.

Abstract

Tumour-induced angiogenesis is one of the six hallmarks of cancer. The localized balance between supply and demand of nutrients and oxygen is disturbed when tumours are formed resulting in tumours receiving less nutrients and oxygen. The hypoxic (lack of oxygen) tumours trigger sprouting until the newly-created capillaries develop a network of blood vessels (through angiogenesis) connecting the tumour to the rest of the cardio-vascular system. This process is affected by an interplay between different cell types, the mechanical stresses in the extracellular matrix (ECM), and the cell signalling networks. Each newly-formed capillary, sprout, is made up of two parts, the tip cell and the stalk cells, with the morphology of the newly-created cells highly dependent on the tip cells' movements. In this thesis I developed one of the first phase-field models of angiogenesis incorporating the mechanics of the phenomenon. In addition, it is the only model to make a connection between the movement of the tip cell and the fracture of the extracellular matrix. Furthermore, the model integrates the biochemical elements into the mechanical progression of the tip.

The solver presented here uses a set of partial differential equations (PDEs) to model different aspects of the phenomenon. This solver consists of three modules; biomechanical, biochemical, and the vascular network module. The biomechanical module is a set of two PDEs. They are the linear momentum balance equation and a phase-field equation for handling the two phases, the endothelial cells (ECs) and the ECM. The constitutive model used here is for anisotropic soft material for both the ECs and the ECM. Energy-based criterion for soft material is used for the fracture of the ECM. Second-order phase-field models are developed here and are discussed with a set of examples.

The second module, biochemical, is made of four advection-diffusion-reaction equations,

each of which is responsible for the concentration of one of the elements involved in the process namely: oxygen, TAF (tumour angiogenesis factor), MMP (matrix metalloproteinases), the ECM (extracellular matrix). The third module, vascular network, describes the movement of the tip cells, possible branching, and anastomosis. Unlike the other modules this module does not have PDEs and instead uses a nonlinear equation solver and a stochastic function to find the location of the tip cell in each step.

The results of this modelling approach conform with the results available from older computational models and experimental models making this work the first model of tumour-induced angiogenesis considering the formation of matrix pathways prior to the migration of the endothelial cells.

Acknowledgements

I would like to thank my supervisor, Prof. Adil Al-Mayah, for his insight and guidance. This research was not possible without his support.

I would also like to thank my dear friend Matin Parchei Esfahani whom I have used his help in a lot of obstacles I faced during the period.

Dedication

To my parents, Fariba and Davood, and Mahsa, who supported me in every step of this work.

Table of Contents

List of Figures

xv

List of Tables

Chapter 1

Introduction

1.1 Importance and motivation

Cancer is the leading cause of death in Canada, accounting for more than thirty percent of deaths in 2012. It is known that one out of every two Canadians is diagnosed with cancer during his/her lifetime [8]. Although cancer is a complex phenomenon, it is stated that six (or eight) hallmarks constitute every cancer case including angiogenesis that is investigated here [9, 10]. Most of cancer research has focused on the biological and biochemical aspects of cancer with little attention to its mechanical aspects. The final goal of this research is to propose a new framework to model angiogenesis which improves the understanding of the phenomenon. The hope is that this framework would help to study what alterations can slow angiogenesis down.

1.2 Problem statement

Tumour-induced angiogenesis is the process of formation of new blood vessels that connects the tumour to the vascular network to supply them with nutrients and oxygen. It is a multi-physics phenomenon that involves secretion of tumour angiogenesis factors (TAFs), degradation and remodelling of the extracellular matrix (ECM), proliferation and directed migration of the endothelial cells towards the tumour cells, branching, anastomosis and formation of loops in the newly-created blood vessels, and finally flow of blood in the vessels. The complete modelling of angiogenesis should take into account the fields of biochemistry, fluid mechanics, and solid mechanics. In this research, a modular solver is written with each of the modules relating to one aspect of angiogenesis. Researchers have developed biochemical and fluid mechanical models in the past, but there are only a handful of models considering the mechanical, biochemical, and biological aspects of the phenomenon. The model proposed here considers all these aspects of angiogenesis thus it is called a chemo-bio-mechanical model.

A modified crack phase-field modelling is applied in this research to model the solid mechanical aspect of the phenomena. It uses a set of partial differential equations (PDEs) to model the deformations and the phase transition. Phase transition shows the migration of endothelial cells in the extracellular matrix. The model also incorporates a set of biochemical advection-diffusion-reaction PDEs to model the biochemical aspect of angiogenesis.

The model presented in this research is the only *in silico* model for tumour-induced angiogenesis which incorporates biochemical equations and biomechanical equations with phase-field analysis which also considers fracture mechanics for the formation of pathways in the extracellular matrix for endothelial cells migration.

1.3 Arrangement of the thesis

The second chapter starts with the biological basis of angiogenesis and continues with a literature review of the computational research done on angiogenesis. It then briefly explains phase-field analysis and provides the work done in this field. The third chapter explains the solver used in this research and then the biomechanical module which includes the endothelial cell migration and the deformations and stresses. The biochemical aspect and the remainder of the theoretical basis are all covered in the fourth chapter. Results from several runs are presented and discussed in chapter five. The last chapter contains the conclusion and mentions several theoretical enhancements to develop the model further.

Chapter 2

Literature Review

Angiogenesis is the formation of a network of blood vessels from pre-existing vasculature [11]. The phenomenon was first observed and described in 1794 by John Hunter. It seems that Flint, JM first coined the term in 1900 while he was describing the vascularization of the adrenal gland [12]. The other method for the formation of new blood vessels is called vasculogenesis. However, it is different from angiogenesis because vasculogenesis is the formation of a network of blood vessels from mesodermal cells in embryogenesis and does not require pre-existing vasculature [13].

There are two main types of angiogenesis from a morphological point of view, namely splitting and sprouting angiogenesis. Splitting (or intussusceptive) angiogenesis is the splitting of an existing blood vessel into two blood vessels caused by external forces from the tissue surrounding the blood vessel [14]. Sprouting angiogenesis, as the name suggests, is the sprouting of a new blood vessel from an existing blood vessel because of an external stimulus [15] (Figure 2.1). A number of phenomena can trigger angiogenesis in capillaries such as tissue-repair, wound healing, female reproductive cycle, and tumour growth [16, 17].
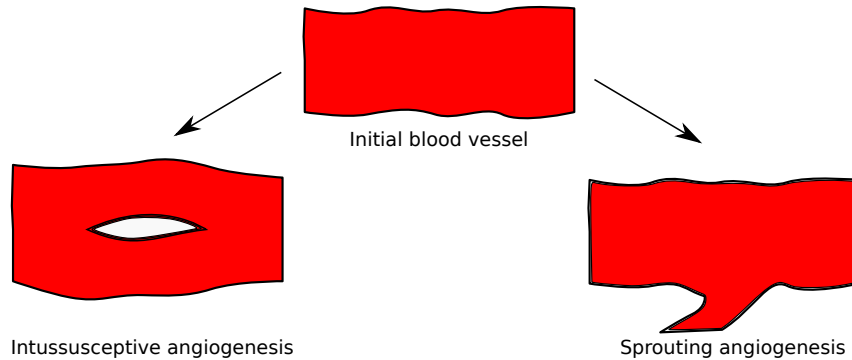
Figure 2.1: Different types of angiogenesis.

The focus of this research is the modelling of the tumour-induced angiogenesis which is a sub-category of sprouting angiogenesis with the proteins secreted from a tumour being the external stimulus for vessel formation [18].

In the first section of this chapter, a brief introduction to the capillaries and tumour-induced angiogenesis is provided. Capillaries are both the pre-existing blood vessels and the final products of angiogenesis. In the second section, a review of the related work conducted in the area of modelling angiogenesis, including their types, components, strength, and weakness are presented. The third section introduces phase-field modelling and its advanced features for modelling angiogenesis.

2.1 Biological aspect of the work

2.1.1 Capillaries

Capillaries are the thinnest and most abundant of the blood vessels which connect the arterioles and venules. The blood flow starts from the heart, the blood full of oxygen

and nutrients goes to aorta, from aorta to arteries, arterioles, capillaries, venules, veins, venae cavae, and from there back to the heart [19]. If the aorta, arteries, veins, and venae cavae are the highways and main streets in the oxygen and nutrient delivery system, the capillaries are the alleys of the system bringing the nutrients to the doorsteps of the tissues and cells. Also, diffusion is how the nutrients and oxygen reach every cell in the body.

Unlike other blood vessels in the human body, the capillaries do not have a lot of structural components such as smooth muscles; they are only made of endothelial cells, basement membrane, and pericytes. The newly formed capillaries in sprouting angiogenesis are mostly made up of endothelial cells, and as the vessels mature, the other two parts are formed in the vessels' walls [19]. Figure 2.2 shows the cross-section of a capillary where endothelial cells line the inner wall of capillaries.

2.1.2 Tumour-induced angiogenesis

Cancer cells are products of several mutations resulting in changes in DNA sequences. One of the significant differences between a cancer cell and a healthy cell is the difference in the rate of cell proliferation and apoptosis; the processes of increasing and decreasing the
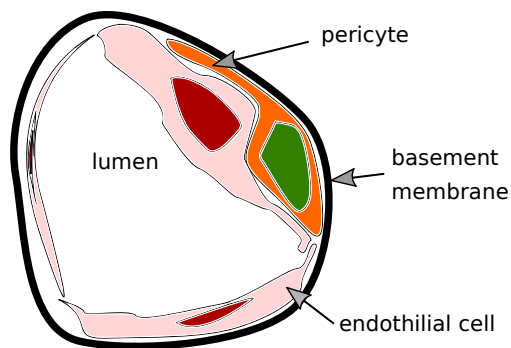
Figure 2.2: A capillary vessel cross section.

6

number of cells, respectively. Proliferation and apoptosis have a balance in healthy cells, so the total number of cells stays constant in adults; in a phenomenon known as homeostasis [20, 21]. This is not the case in cancer cells, the mutations increase the proliferation rate and decrease the apoptosis rate so the tumour will grow compared to the surrounding tissues [9, 22]. The vasculature in the body is designed to be sufficient for our bodies in typical situations. When a tumour grows in the human body, the distance of some of the tumour cells from the blood vessels becomes more than the penetration depth; the depth that oxygen and nutrients can diffuse in the extracellular matrix (ECM) [23, 24]. This would generally happen when the tumour diameter exceeds 2 to 3mm [25]. The cells in the middle of a tumour now lack oxygen and nutrients causing them to become hypoxic [26]. Hypoxia is dangerous to both healthy and cancer cells but as explained below, the malignant cells have a way to overcome this lack of resources [27].

The tumour stops growing because of this lack, and the hypoxic cells start excreting proteins called tumour angiogenesis factors (TAF) [28]. Most significant sub-group of TAF proteins are named vascular endothelial growth factor (VEGF) [29]. These proteins will spread in the tumour's surrounding causing a concentration gradient of TAF towards the tumour. The receptors on the endothelial cells will recognize these proteins, and the endothelial cells will start moving towards the TAF's gradient [30]. This process of cells moving towards a higher concentration of soluble molecules is called chemotaxis [31]. Cell migration results in sprouting and the movement of the sprout towards the tumour. The sprout consists of two main parts; tip cell and stalk cells. The tip cell is the cell moving because of chemotaxis, haptotaxis[1], etc. while the stalk cells are the ones following the

---

[1]Haptotaxis is the directional movement of cells towards the higher values of cellular adhesion in the ECM [32]. The term haptotaxis was first coined in 1967 by Carter [33]. Fibronectin present in the ECM causes haptotaxis in angiogenesis [34]. At first, it was thought chemotaxis is a subset of haptotaxis but
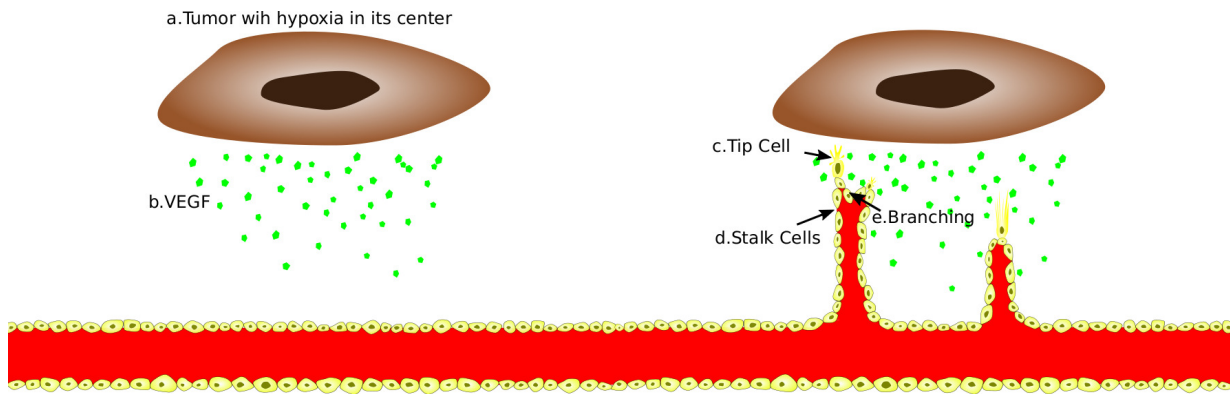
Figure 2.3: Sprouting angiogenesis progress: a) Oxygen and nutrients not reaching the deep cells in tumour resulting in hypoxia. b) Hypoxic cancer cells secreting TAF creating a TAF concentration towards the tumour. c) Tip cells start moving toward the higher gradient, the tumour, called chemotaxis. d) Stalk cells following the tip cell because of cell adhesion. e) Formation of two sprouts from one. The sprouts finally reach the tumour cell and the tumour starts to grow again.

tip cell because of the cell adhesion forces [37]. The VEGF molecules also increase the proliferation rate in the endothelial cells providing the needed cells for sprout elongation [31]. One other significant effect of VEGF on the sprouts is that it causes the tip cell to excrete enzymes with the name of matrix metalloproteinase (MMP). These enzymes will degrade the surrounding ECM and would eventually help the tip cell to penetrate through it [38, 39, 40]. Different sprouts might merge into one. This phenomenon is called anastomosis. Anastomosis results in loop formation and blood flow in the loops. Also, one sprout can branch into two sprouts called branching.

When the sprouts reach the tumour, and a whole network of new blood vessels is constructed, blood would start flowing, and hence the tumour will receive its needed nutrients

later on this hypothesis was rejected [35]. For more information on haptotaxis, please refer to [36].

and oxygen allowing the tumour to resume its growth. All angiogenesis processes can be seen in Figure 2.3.

There is another important feature of angiogenesis not discussed above, and that is ECM remodelling [19]. Before the movement of the endothelial cells in the extracellular matrix, traction forces exerted by the ECs align the collagen fibres in the ECM along the cell migration path [41].

2.2 Previous models of angiogenesis

There are three main approaches to model angiogenesis in cancer; continuous, discrete, and hybrid [42]. Continuum modelling is the oldest of them and is the framework used in this research. All three approaches are merely constructed by solving a system of partial differential equations (PDEs). One of the earliest works done using the continuous method is the paper by Zawicki in 1981 [43]. The first models were mostly one-dimensional models not covering the morphological aspects of angiogenesis like branching or anastomosis [16]. They were mostly a system of two PDEs, one for the density of endothelial cells and the other for the concentration of the chemical stimulus (TAF) for cell migration.

The first comprehensive in-silico model of tumour-induced angiogenesis was introduced by Anderson in 1998 [30]. This model incorporated a system of three PDEs; one for EC density, one for the concentration of TAF, and the last for fibronectin (FN) concentration. The model proposed both continuous and discrete approaches for solving the system of PDEs. The continuous model only showed the average density of the endothelial cells and could not show the visual illustration of the network of the vessels created by angiogenesis. However, the discrete approach succeeded in showing the morphological aspect of angiogenesis and added three simple algorithms to account for branching, anastomosis,

and EC proliferation. The discrete approach was widely used in recent literature. The continuous framework we are using in this research incorporates the Ginzburg-Landau type equations for phase-field modelling to implement both the continuum approach and the morphological properties of angiogenesis. More on our approach will be discussed later.

Newer models added more PDEs to account for other aspects of angiogenesis like the evolution of MMP level, the ECM degradation by MMP [38], and the effect of the ECM's oxygen level on angiogenesis. However, all the models discussed to this point are purely biochemical models not accounting for other aspects of tumour-induced angiogenesis like fluids and solid mechanics. As mentioned before, anastomosis leads to loop formation and flow of blood in the loops. The blood pressure increases the blood vessel diameter, and flow of blood brings oxygen and nutrients to the tumour. The first models that also covered the blood flow in the newly created capillaries during angiogenesis were presented by McDougall [44, 26] where blood flow in the capillaries was modelled using a Poiseuille-like expression with a nonlinear viscosity. In these models, the effect of the fluid mechanics module on the model was limited to initiating new branches.

Migrating cells need to exert traction forces on the ECM to be able to move in a multi-step process of cell migration. First, the cell senses the stimuli for movement using the filopodia. Second, the cell extends and forms protruding lamellipodia. It attaches the protruded parts to the ECM. Then, the cell contracts using its radial fibres. These radial fibres are connected to finger-like structures on the cell wall holding the cell to the ECM. It later tears the fibres in the back apart allowing the cell to move forward. To model this sophisticated phenomena, it is essential to include a biomechanical engine in our angiogenesis model [45]. One of the earliest attempts to model the interaction between a cell and the ECM mathematically was presented by Murray in 1984 [46]. Also, the interaction between the two in cell movement in angiogenesis was modelled by Manoussaki

in 1996 [47] and Holmes in 2000 [48]. These papers assumed viscoelastic material properties using Kelvin-Voigt model which is represented by a parallel system of a linear elastic spring and a dashpot [49, 50]. The mechanical stresses affect both the path and the speed of angiogenesis.

There is another way to model the migration of the tip cell in angiogenesis. This approach uses empirical formulas for the speed of the tip cell which is related to the other parameters, like the concentration of chemotactic and haptotactic stimuli or maximum stress, which are calculated using the other PDEs. For further discussion on this approach refer to [1, 5].

2.3   Phase-field modelling of crack propagation

The phase-field method is a method to solve non-equilibrium systems problems by converting the discontinuous interfaces into continuous functions. Used primary in material science and physics community, the framework was used in solving the problems with a moving phase boundary [51]. Researchers studied the motion of phase boundaries since the early 1800s. The problem was first solved in the 1890s by Josef Stefan [52]. At first, the sharp interfaces were used for the movement of the boundary as seen in the green plot shown in Figure 2.4; more on the figure in the next chapter. Unlike the second (red) and fourth-order (blue) plots shown in the figure, these discontinuities were hard to implement. Therefore to make it solvable using partial differential equations, some phase-field parameters, such as d, were assigned to the domain. The phase-field parameter can have two types; conserved or non-conserved. For the conserved phase-field variables, Cahn-Hilliard [53] equation is used to describe the evolution of the variable (Eq. 2.1), and for non-conserved, Allen-Cahn [54] equation (Eq. 2.2) or the time-dependent Ginzburg-Landau
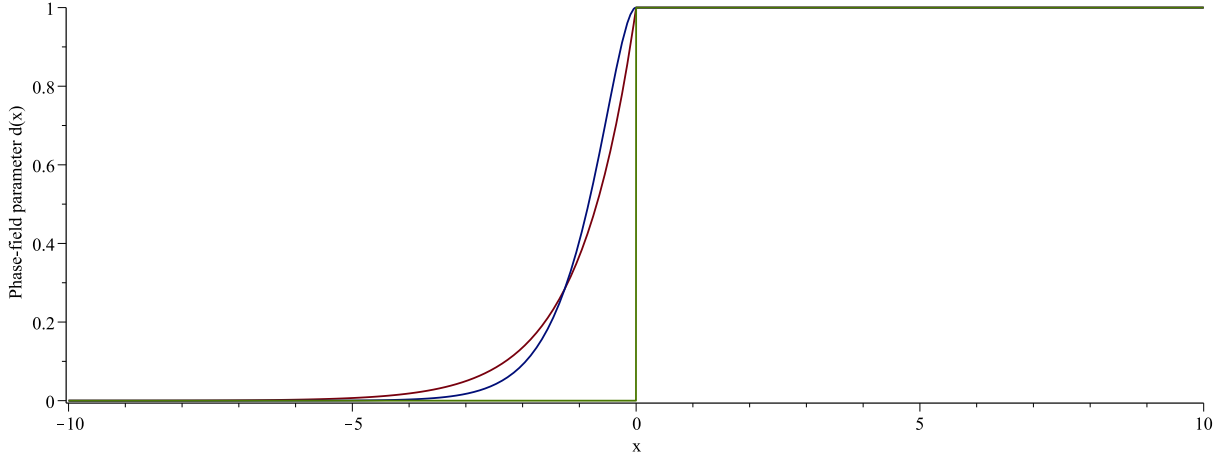
Figure 2.4: Three different plots for the phase transition, the phase field parameter, d, is defined to be between zero and one, where zero means that the point in the domain purely consists of the extracellular matrix and one suggests that the point is occupied entirely with endothelial cells. In the phase-field analysis, instead of the discontinuous transition between the two phases, a continuous function is assumed, the red one is called a second-order phase-field function and is a continuous function but not differentiable at the point x=0, the blue one is a fourth-order function and is a differentiable function throughout the domain. In all the plots $l = 1$ is assumed.

type equation is used.

In equations

$$\frac{\partial c_i}{\partial t} = \nabla M_{ij} \nabla \frac{\delta F}{\delta c_j(r,t)} \tag{2.1}$$

and

$$\frac{\partial \eta_p}{\partial t} = -L_p \nabla \frac{\delta F}{\delta \eta_p(r,t)} \tag{2.2}$$

r is the location and t is the time, F is the free energy level of the system, c_n and η_p are the conserved and non-conserved field variables, M_i and L_p are the diffusivity and the mobility

coefficients respectively [55].

A method similar to the one used in fracture modelling is applied to have two phases in this research. Early work conducted by Griffith [56] and Irwin [57] proposed the base theories and fundamentals of brittle fracture. However, Franc and Margio [58] made the first attempts to model brittle fracture using phase-field method and energy minimization in 1998 that was faced with the challenge of thermodynamic stability issue. A decade later, Miehe proposed a method for brittle fracture modelling which was also thermodynamically stable [2, 59]. Many shortcomings in Griffith's method for crack modelling are addressed in the proposed phase-field models. Recently, Rania and Miehe proposed a phase-field method to model fracture in biological tissues [60]. Further improvements was made by Gültekin [3, 61] to model highly anisotropic material using constitutive models proposed by Holzapfel and Gasser [62, 63].

To the author's knowledge, there is limited research effort that applied continuous mechanical phase-field modelling approach for angiogenesis [51]. The main deficiency of these models are the linear elastic material assumption, no network formation, and limited biochemical integration. All the problems above will be addressed in our new model plus a feature not present in any other papers on angiogenesis. The modelling of the ECM remodelling and formation of matrix pathways using the equations of failure and crack propagation in soft materials prior to the ECs penetrating in the ECM.

2.4   Conclusion

Few attempts have been made to develop a biomechanical model of the angiogenesis. Most of the attention has been paid to the biochemical aspect of angiogenesis. There are semi-discrete/semi-continuous phase-field models for modelling angiogenesis, but those models

do not incorporate the mechanical aspects of the phenomenon [64]. However, the integration of these two, biomechanical and biochemical, has a great potential to realistically model the process of angiogenesis which can result in a better understanding of the phenomenon and later, this new mechanical oriented view on cancer can help creation of new treatments for cancer.

Therefore, the proposed model in this research utilizes a modified fracture phase-field modelling approach for modelling the matrix pathways in the extracellular matrix coupled with a system of PDEs to account for a wide range of biochemical reactions in angiogenesis. It also incorporates some advanced features to model the capillary formation. All are discussed in the next chapter and chapter four.

Chapter 3

Biomechanical Module

This chapter first discusses the big picture of the solver used in this research. It then presents the biomechanical aspect of the solver, the base formulas, their derivation, and the numerical implementation.

3.1 Solver components

The solver used in modelling of angiogenesis consists of three modules to solve three physical aspect of angiogenesis. They are the biomechanical, the biochemical, and the vascular network module as shown in figure 3.1A. As illustrated in the figure, the solver starts with the biochemical module, it calculates the values for the four biochemical variables, the concentration of oxygen, TAF, and matrix degrading enzymes (MDE), and the density of the ECM, in each time step. Then, these values are incorporated into the biomechanical module which calculates the values for deformations, stresses, and phase change. This module solves a nonlinear system of PDEs which requires nonlinear finite elements to be

implemented using the Newton-Raphson method for each time step. This requires a set of iterations in each time step for the biomechanical module. One iteration is shown in Figure 3.1B. After the second module execution, the results are passed to the third module, the vascular network module. This module checks if there is a need for updating the location of the tip cell and if so, it uses the Newton-Raphson method to find the location of the next tip cell. The module then checks for branching and anastomosis and starts the biochemical module for the next time step. The analysis is complete when the newly-constructed blood vessel reaches the tumour.

In the next sections of the chapter, we will address the formulas and their derivations in the biomechanical module.

3.2   The biomechanical module

This module is the most comprehensive module in the analysis and takes most of the runtime for the solver. It uses the large deformation, soft material properties, and anisotropic formulas mainly derived from Bower [65] and Holzapfel and Gasser [63, 62]. This module consists of two main PDEs in the Lagrange-Euler equations format. One of them is the equation governing the balance of linear momentum, and the other one is the equation determining the topology of the diffusive phase transfer.

As seen in Figure 3.1B, this module consists of three steps in each iteration, the first step solves the balance of linear momentum PDE and outputs the values for deformations, the second step calculates the values for the history function which is the connection between the two PDEs. The last step uses the values of the history function to solve the phase transfer PDE. The loop would run until the convergence criterion is met.
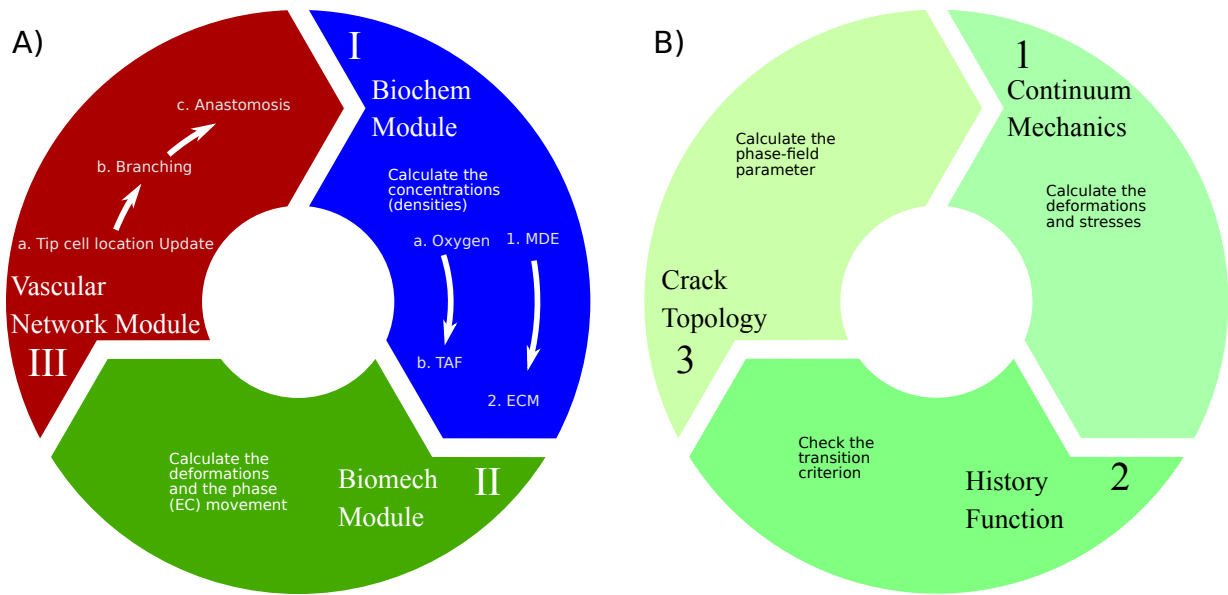
Figure 3.1: The flow diagram representing the different modules in the solver. A: The three main modules building up the solver. The solver starts with the biochemical module (module I) that calculates the concentration of oxygen and MDE in the domain and implements their values to calculate the TAF level and the density of the ECM respectively. Module I feeds the values of concentrations to the biomechanical module (module II). This module calculates the deformation, the stresses, and the phase movement as shown in B. Vascular network module (module III) updates the tip cell location and checks for branching and anastomosis. After the third module's execution, the solver proceeds to the next time step. B: This figure is the flow diagram of the second module. At first, the continuum mechanics sub-module is run to find the deformations and the stresses throughout the domain. Then the history function is executed in all Gaussian points to find in which, the phase transition has started. Then the phase-field PDE is solved to calculate the movement of EC in the ECM.
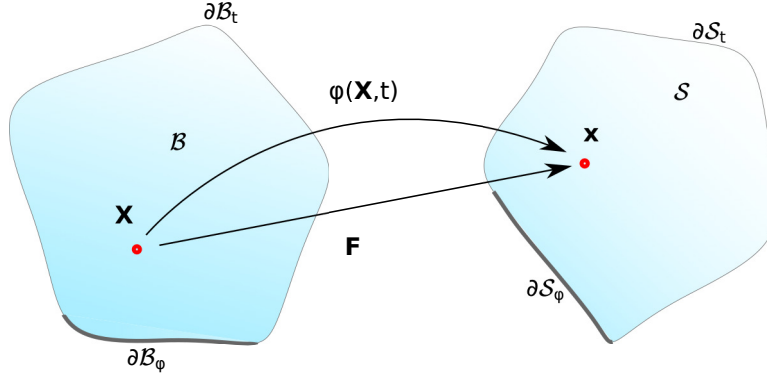
Figure 3.2: Large deformation of a solid. The solid has the initial configuration $\mathcal{B} \subset \text{Re}^n$ and deforms because of the external forces to $\mathcal{S} \subset \text{Re}^n$ at time $t \in \mathcal{T} \subset \text{Re}$. $\boldsymbol{\varphi}$ maps the points on $\boldsymbol{X}$ to $\boldsymbol{x}$ and $\boldsymbol{F}$ is the material gradient of $\boldsymbol{\varphi}$.

In the following sections, the phase variables, large deformations continuum mechanics and diffusive cracks are introduced. In the fifth section, we discuss the constitutive equations used in this model, hyperelasticity and anisotropicity. The sixth section is about the active stress causing the cell migration. Then we focus on deriving the main Euler-Lagrange PDEs. This is followed by a brief description of cell proliferation and the phase change equations in section ten. The last part will present the matrix form of equations.

3.3   Field variables

Consider a deformable body at the time $t = 0$, the body is said to be in the reference configuration at this time. The reference configuration is defined in an n-dimensional setting by $\mathcal{B} \subset \text{Re}^n$ and the material points are designated with $\boldsymbol{X} \in \mathcal{B}$ as depicted in Figure 3.2. The surface of $\mathcal{B}$ is defined as $\partial \mathcal{B} \subset \text{Re}^{n-1}$. In the same matter, the deformed body at any time except the initial time (*i.e.* $t \neq 0 \mid t \in \mathcal{T} \subset \text{Re}$) is defined by

$\mathcal{S} \subset \mathrm{Re}^n$. This configuration is called the spatial configuration and its surface is depicted as $\partial\mathcal{S} \subset \mathrm{Re}^{n-1}$. The transformation function mapping the material points to the spatial point is called the deformation map $\boldsymbol{\varphi}(\boldsymbol{X}, t)$. The deformation map is defined as

$$\boldsymbol{\varphi}_t(\boldsymbol{X}) : \begin{cases} \mathcal{B} \times \mathcal{T} \to \mathcal{S}, \\ (\boldsymbol{X}, t) \mapsto \boldsymbol{x} = \boldsymbol{\varphi}(\boldsymbol{X}, t). \end{cases} \tag{3.1}$$

The other main field variable is the phase-field parameter $d(\boldsymbol{X})$. The parameter is defined on the entire reference configuration, $\mathcal{B}$, and evolves as time proceeds. The phase-field parameter of one represents an intact state, *i.e.* the extracellular matrix being untouched, and zero represents cracked, *i.e.* endothelial cells moving into the ECM. As apparent in Figure 2.4 there are several ways to make the transition between the two phases continuous. The red plot is a second-order phase-field function, and the blue one is a fourth-order function as apparent in Figure 2.4. Intuitively, it can be concluded that any values between zero and one would mean that the material point is in the process of phase transition. The phase-field parameter is defined as

$$d_t(\boldsymbol{X}) : \begin{cases} \mathcal{B} \times \mathcal{T} \to [0, 1], \\ (\boldsymbol{X}, t) \mapsto d = d(\boldsymbol{X}, t). \end{cases} \tag{3.2}$$

3.4 Large deformations main formulas

Biological tissues experience large deformations when subjected to external forces. The continuum framework used in this research incorporates large deformations and nonlinear geometry. Let's start the discussion by defining the two different types of the gradient. The material gradient is the gradient with respect to the reference configuration, and the spatial gradient is the gradient with respect to the spatial coordinates. Equations 3.3 and

3.4 show the two kinds of gradient respectively.

$$\nabla_X \square = \nabla \square = \square_{,\boldsymbol{X}} = \frac{\mathrm{d}\square}{\mathrm{d}\boldsymbol{X}} \tag{3.3}$$

$$\nabla_x \square = \square_{,\boldsymbol{x}} = \frac{\mathrm{d}\square}{\mathrm{d}\boldsymbol{x}} \tag{3.4}$$

in these equations, $\square$ (square) can be replaced by any investigated variable.

The first tensor to be defined in this framework is the deformation gradient tensor which is the material gradient of the deformation map which can be depicted in matrix form as

$$\boldsymbol{F} = \nabla\boldsymbol{\varphi} = \boldsymbol{\varphi}_{,\boldsymbol{X}} = \frac{\mathrm{d}\boldsymbol{\varphi}}{\mathrm{d}\boldsymbol{X}} = \frac{\mathrm{d}\boldsymbol{x}}{\mathrm{d}\boldsymbol{X}} \tag{3.5}$$

and using the index notation it can be depicted as

$$F_{ij} = \frac{\partial x_i}{\partial X_j} = \delta_{ij} + \frac{\partial u_i}{\partial X_j}. \tag{3.6}$$

This tensor relates fibers' length in the initial configuration to their length in the spatial configuration; $\mathrm{d}\boldsymbol{x} = \boldsymbol{F}\mathrm{d}\boldsymbol{X}$. The Jacobian of the deformation tensor relates the initial, $\mathrm{d}V$, and the spatial, $\mathrm{d}v$, infinitesimal volumes

$$J = \det(F) \qquad \mathrm{d}v = J\mathrm{d}V. \tag{3.7}$$

The deformation gradient is unsymmetrical so the right, $\boldsymbol{C}$, and the left, $\boldsymbol{b}$, Cauchy-Green tensor, or the Green and Cauchy deformation tensors respectively, are defined as

$$\boldsymbol{C} = \boldsymbol{F}^T\boldsymbol{F}, \quad C_{ij} = F_{ki}F_{kj} \tag{3.8}$$

$$\boldsymbol{b} = \boldsymbol{F}\boldsymbol{F}^T, \quad b_{ij} = F_{ik}F_{jk}. \tag{3.9}$$

The first tensor utilizes the Lagrangian configuration and the second one uses the Eulerian configuration. There are n tensor invariants for a second-order tensor in an n-dimensional

20

space. The three invariants for the matrix b are as follows:

$$I_1 = \text{tr}(\boldsymbol{b}) = b_{kk}, \quad I_2 = 1/2[I_1^2 - \text{tr}(\boldsymbol{b}^2)] = 1/2[I_1^2 - b_{ik}b_{ki})], \quad I_3 = \det(\boldsymbol{b}) = J^2. \quad (3.10)$$

When the material is incompressible, as it the case with biological tissues, three other invariants are used instead of the ones in 3.10. The new invariants are

$$\bar{I}_1 = \frac{I_1}{J^{(2/3)}}, \quad \bar{I}_2 = \frac{I_2}{J^{(4/3)}}, \quad J = \sqrt{\det(\boldsymbol{b})}. \quad (3.11)$$

Note that $J \approx 1$ in incompressible materials because $\text{d}v \approx \text{d}V$.

The soft material used in the modelling is anisotropic. It means it has different characteristics in different directions. There are two preferred directions in which the material behaves stiffer. The two are shown with the vectors M and M'. In the deformed material they have the preferred directions m and m' as shown in the Figure 3.4. More information about the anisotropic behaviour is given in Section 3.6. The deformed preferred directions are calculated as

$$\boldsymbol{m} = \boldsymbol{FM}, \quad \boldsymbol{m}' = \boldsymbol{FM}', \quad \text{or} \quad m_{ij} = F_{ik}M_{kj}, \quad m'_{ij} = F_{ik}M'_{kj}. \quad (3.12)$$

The preferred directions can be shown in tensor form as

$$\boldsymbol{A_m} = \boldsymbol{m} \otimes \boldsymbol{m}, \quad \boldsymbol{A_{m'}} = \boldsymbol{m}' \otimes \boldsymbol{m}' \quad \text{or} \quad A_{ij}^m = m_i m_j \quad A_{ij}^{m'} = m'_i m'_j. \quad (3.13)$$

As mentioned in [62, 63, 66], five other pseudo-invariants can be used for the isotropic media with two preferred directions which only two of them would be considered here. The two are

$$I_4 = \boldsymbol{m} \cdot \boldsymbol{m}, \quad I_6 = \boldsymbol{m}' \cdot \boldsymbol{m}', \quad \text{or} \quad I_4 = m_i m_i, \quad I_6 = m'_i m'_i, \quad (3.14)$$

21
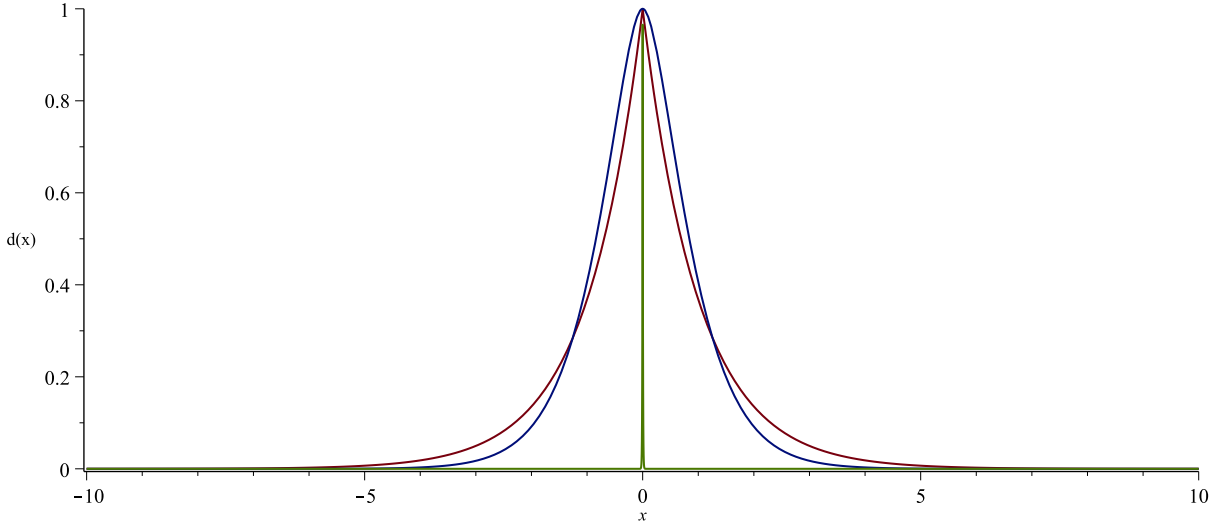
Figure 3.3: The phase-field representation of a line of endothelial cells at $x = 0$ and extracellular matrix at $\pm\infty$ for a length-scale parameter equal to one. The green plot uses Kronecker delta function for describing the different phases 3.15, the red and blue plots use 3.16 and 3.17 respectively. The left side of the plots are the same as Figure 2.4.

3.5   Diffusive crack

As mentioned before, the main difference between the modelling approach used here and the ones used in the previous biomechanical models is the implementation of fracture-based phase-field modelling for the phase transformation[1]. Ginzburg-Landau type equations would be used to describe the phase-field over the domain.

First, let's assume an infinite one-dimensional medium $L = [-\infty, +\infty]$ fully made of the extracellular matrix $d = 0$. Endothelial cells are only present at $x = 0$. The classical

---

[1]Only [51] implemented the phase-field modelling without integrating the fracture mechanics.

method to define the two phases is by use of the Kronecker delta function

$$d(x) = \delta_{ij,j=0} = \delta(x) = \begin{cases} 1 & x = 0 \\ 0 & x \neq 0. \end{cases} \tag{3.15}$$

The equation above looks like the Dirac delta function (green plot in Figure 3.3). The problem is that this formula contains discontinuities which may cause numerical problems in solving the differential equations[2]. To overcome the discontinuities, diffusive transition would be assumed so the phase transition would be gradual throughout the domain. The red plot in figure 3.3 is a second-order phase-field function which is continuous throughout the domain and differentiable in all points except $x = 0$ as represented in equation 3.16.

$$d(x) = e^{-|x|/l}. \tag{3.16}$$

To have a phase-field equation which is differentiable throughout the domain the blue plot can be used which is a fourth-order phase-field equation (3.17). It reduces the numerical problems and is the best approach for isogeometric analysis [70, 71].

$$d(x) = e^{-2|x|/l}(1 + \frac{2|x|}{l}). \tag{3.17}$$

In the two equations 3.16 and 3.17, l is the length-scale of the transition topology. It shows how wide the phase transition is. If $l \to 0$, it results in the green plot in Figure 3.3.

These two equations can be transformed into ordinary differential equations (ODEs) with Dirichlet-type boundary conditions given below respectively.

$$d(x) - l^2 d''(x) = 0, \qquad d(0) = 1, \quad d(\pm\infty) = 0. \tag{3.18}$$

---

[2] Phase-field analysis turns the discontinuity into continuity and the solves the problem. Alternatively, extended finite element [67, 68] or phantom nodes [69] like approaches should be implemented to facilitate solving the problem.

$$d(x) - \frac{l^2}{2}d''(x) + \frac{l^4}{16}(d^{(4)}(x)) = 0, \qquad d(0) = 1, \quad d'(0) = 0, \quad d(\pm\infty) = 0. \qquad (3.19)$$

As seen above, 3.18 is a second-order ordinary differential equation and 3.19 is a fourth-order ODE which explains the naming for equations 3.16 and 3.17 respectively.

The formulas above can be transformed to Euler-Lagrange equations of the variational principle for the second-order equation,

$$d = \text{Arg}\left\{\inf_{d\in\mathcal{W}_d} I(d)\right\}, \qquad \mathcal{W}_d = \{d \mid d(0) = 1, d(\pm\infty) = 0\}$$

$$I(d) = \frac{1}{2}\int_{\mathcal{B}}(d^2 + l^2(d')^2)dx, \qquad (3.20)$$

and for the fourth-order equation,

$$d = \text{Arg}\left\{\inf_{d\in\mathcal{W}_d} I(d)\right\}, \qquad \mathcal{W}_d = \{d \mid d(0) = 1, d'(0) = 0, d(\pm\infty) = 0\}$$

$$I(d) = \frac{1}{2}\int_{\mathcal{B}}(d^2 + \frac{l^2}{2}(d')^2 + \frac{l^4}{16}(d'')^2)dx. \qquad (3.21)$$

The formulas 3.20 and 3.21 can be written in three-dimensional space in equations 3.22 to 3.25 respectively.

$$d(\boldsymbol{X}, t) = \text{Arg}\left\{\inf_{d\in\mathcal{W}_{\Gamma}(t)} \Gamma_l(d)\right\},$$

$$\mathcal{W}_{\Gamma(t)} = \{d \mid d(\boldsymbol{X}, t) = 1 \text{ @ } \boldsymbol{X} \in \Gamma(t)\}, \qquad (3.22)$$

$$\Gamma_l(d) = \int_{\mathcal{B}}\gamma(d, \nabla d)dV,$$

$$\gamma(d, \nabla d) = \frac{1}{2l}(d^2 + l^2 \mid \nabla d \mid^2). \qquad (3.23)$$

$$d(\boldsymbol{X}, t) = \text{Arg}\Big\{ \inf_{d \in \mathcal{W}_\Gamma(t)} \Gamma_l(d) \Big\},$$

$$\mathcal{W}_{\Gamma(t)} = \{d \mid d(\boldsymbol{X}, t) = 1, \nabla d(\boldsymbol{X}, t) = 0 \ @ \ \boldsymbol{X} \in \Gamma(t)\}, \tag{3.24}$$

$$\Gamma_l(d) = \int_{\mathcal{B}} \gamma(d, \nabla d, \Delta d) dV,$$

$$\gamma(d, \nabla d, \Delta d) = \frac{1}{2l}(d^2 + \frac{l^2}{2} \mid \nabla d \mid^2 + \frac{l^4}{16} \mid \Delta d \mid^2). \tag{3.25}$$

In the formulas above, Δ is the Laplacian and is defined as $\Delta \square = \nabla^2 \square = \nabla \cdot \nabla \square$. Also, γ is called the volume specific transition surface. By minimizing the two variational forms above in three-dimensional space, the Euler-Lagrange partial differential equation

$$d - l^2 \Delta d = 0 \quad \text{in } \mathcal{B} \quad \text{while} \quad \nabla d \cdot \boldsymbol{N} = 0 \quad \text{on } \partial \mathcal{B} \tag{3.26}$$

would be obtained for 3.22 and

$$d - \frac{l^2}{2}\Delta d + \frac{l^4}{16}\Delta^2 d = 0 \quad \text{in } \mathcal{B}$$

$$\text{while} \quad \Delta d = 0 \quad \text{and} \quad [\frac{l^2}{8}\nabla(\Delta d) - \nabla d] \cdot \boldsymbol{N} = 0 \quad \text{on } \partial \mathcal{B} \tag{3.27}$$

would be obtained for 3.24. In the formulas above, $\boldsymbol{N}$ is the normal vector to $\partial \mathcal{B}$. In this research project, the second-order formulas are used because of the lower computational cost and the implementation of the classic finite element method shape functions instead of the ones introduced in isogeometric analysis or the higher-order finite element method.

3.6 Constitutive model

The biological tissues are categorized into two types; soft tissues and hard tissue [72]. Hard tissues are mostly bones and teeth, and soft tissues are the rest of the tissues in the body.

Soft tissues consist of muscular, epithelial, nervous, and some of the connective tissues. Arterial tissues', a subgroup of muscular tissues, properties are used in this research for modelling of the endothelial cells' and the extracellular matrix's mechanical response. In this section, a brief explanation of the soft tissues characteristics will be presented first, followed by the energy function and its derivatives.

3.6.1 Soft tissue's mechanical characteristics

Hyperelasticity

The two-word definition for hyperelasticity is "nonlinear elastic." So the strain-stress curve is nonlinear, but the loading and unloading happen on the same curve. There is no need for hysteresis, and only an energy function and a value for stress is enough to find the strain at any given time.

Anisotropicity

Anisotropicity is a material having different material properties in different directions. In blood arteries, there are some preferred directions which the soft material, both the blood vessels and the extracellular matrix, behaves stiffer in those directions. This behaviour is because the biological tissues are constituted of different materials which the main ones are elastin and collagen proteins. Elastin behaves the same in every direction, and "is the most linear elastic of the biosolid materials known" [73]. On the other hand, collagen fibres only act in certain directions and cause the anisotropicity. A good analogy is to compare the vessel wall with a reinforced concrete member. Elastin acts isotropically like concrete with the difference of acting both in compression and tension. On the other hand,

a collagen fibre works better in one direction just like the steel rebars with one difference that collagen fibres only work in tension. The other difference is that in the vessel wall, there is an infinite number of rebars in the selected directions. Recent studies indicate that the number of preferred directions are different in different tissues [74]. Figure 3.4 shows a tissue with two preferred directions before and after the deformation.

Heterogeneity

Heterogeneity is the state of having diverse properties at different points of the material. The ECM and blood vessels are mostly defined by the average values of their mechanical properties, but yet they are highly heterogeneous [24].

Incompressibility & viscoelasticity

Soft tissues are considered nearly incompressible because of their high water content. They are also considered viscoelastic because their behaviour is a function of time [75, 76].

Hyperelasticity, anisotropicity, and incompressibility are recognized in the constitutive model discussed below.

3.6.2 Formulization

As mentioned before, the energy function alone is enough to describe the mechanical behaviour of hyperelastic materials. The energy function is constituted of two parts, an isotropic term for the elastin proteins and an anisotropic term for the collagen fibres' effect. The isotropic term is a function of deformation invariants discussed in 3.11. Simple material models, like the Neo-Hookean model [77, 78], make use of only $\bar{I}_1$ and J. For the

27

anisotropic term, only two pseudo-invariants are used, each of the invariants is for one of the fibre directions. The energy function is

$$\Psi_0 = \Psi_0(\boldsymbol{F}, \boldsymbol{A_m}, \boldsymbol{A_{m'}}) = \Psi_0^{iso}(J, \bar{I}_1) + \Psi_0^{ani}(I_4, I_6) = \Psi_0^{iso}(J, \bar{I}_1) + \Psi_0^{ani}(I_4, I_6), \tag{3.28}$$

$$\Psi_0^{iso}(J, I_1) = \frac{\mu_1}{2}(\bar{I}_1 - 3) + \frac{K_1}{2}(J - 1)^2, \tag{3.29}$$

$$\Psi_0^{ani}(I_4, I_6) = \frac{k_1}{2k_2} \sum_{i=4,6} \{\exp\big(k_2(I_i - 1)^2\big) - 1\}. \tag{3.30}$$

The anisotropic term is based on [62] and defines an exponential function for each fibre direction which behaves stiffer as the strain values go higher. Here, μ_1 is the shear modulus and K_1 is the penalty parameter and the higher it is, the more incompressible the material is. The parameters k_1 and k_2 are material constants. Note that μ_1, K_1, and k_1 have the unit of stress while k_2 is dimensionless. Also, only the values over 1 for I_4 and I_6 are considered because the collagen fibres work only when the fibre is engaged in tension. If the fibres go through compression and each of the pseudo-invariants go under 1, the related term for anisotropic energy would be zero. So, if the values for both I_4 and I_6 are less than 1, the material would behave completely isotropic. The preferred directions are shown in Figure 3.4 in both initial and spatial configurations.

Passive true stress $\bar{\sigma}_{ij}$ and passive Kirchhoff stress $\bar{\tau}_{ij}$ are defined as

$$\bar{\sigma}_{ij} = \frac{1}{J} F_{ik} \frac{\partial \Psi}{\partial F_{jk}} \quad \text{and} \quad \bar{\tau}_{ij} = J\bar{\sigma}_{ij} = F_{ik} \frac{\partial \Psi}{\partial F_{jk}}. \tag{3.31}$$

Inserting the equations 3.29 and 3.30 in 3.31 results in

$$\bar{\tau}_{ij}^{iso,0} = \frac{\mu_1}{J^{2/3}}\Big(B_{ij} - \frac{1}{3}B_{kk}\delta_{ij}\Big) + K_1 J(J - 1)\delta_{ij} \tag{3.32}$$

and

$$\bar{\boldsymbol{\tau}}^{ani,0} = 2\psi_{,4}\boldsymbol{m} \otimes \boldsymbol{m} + 2\psi_{,6}\boldsymbol{m'} \otimes \boldsymbol{m'}, \quad \bar{\tau}_{ij}^{ani,0} = 2\psi_{,4}m_i m_j + 2\psi_{,6}m'_i m'_j. \tag{3.33}$$
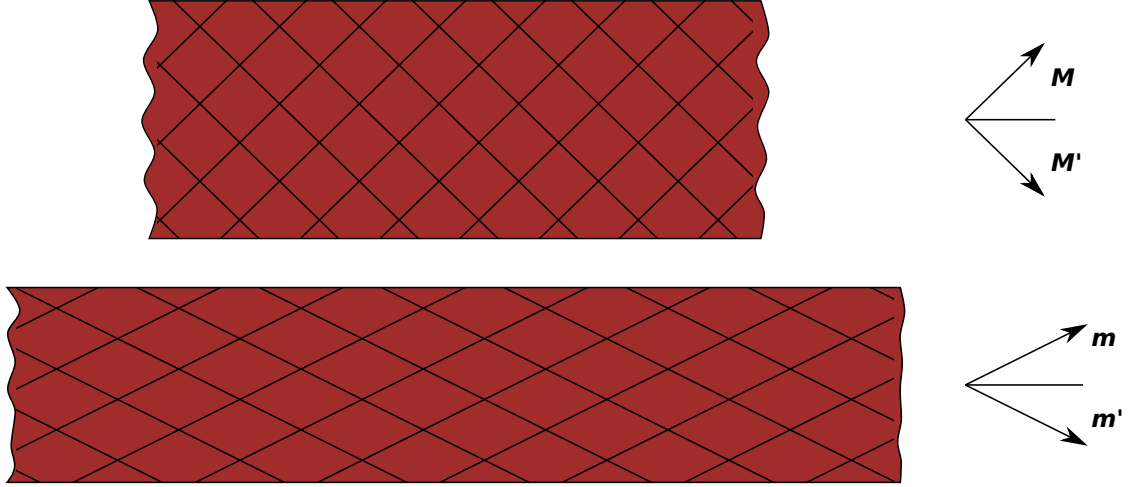
Figure 3.4: The top figure shows the anisotropic material in nondeformed configurations with two preferred directions $\boldsymbol{M}$ and $\boldsymbol{M}'$. The bottom figure shows them in the spatial configuration with the two directions $\boldsymbol{m} = \boldsymbol{FM}$ and $\boldsymbol{m}' = \boldsymbol{FM}'$. Red shows the elastin protein which governs the isotropic response of soft tissues.

In equation 3.33 $\psi_{,i=4,6}$ is the derivative of the energy function with respect to the psuedo-invariants

$$\psi_{,i=4,6} = \partial_{I_i} \Psi_0 = k_1(I_i - 1) \exp\big(k_2(I_i - 1)^2\big). \tag{3.34}$$

The tangent stiffness tensor or the Eulerian elasticity tensor is defined as

$$C_{ijkl} = \frac{\partial \tau_{ij}}{\partial F_{km}} F_{lm} = J\sigma_{ij}\delta_{kl} + J\frac{\partial \sigma_{ij}}{\partial F_{km}} F_{lm}. \tag{3.35}$$

So using the same approach the isotropic and the anisotropic terms are

$$C_{ijkl}^{iso,0} = \frac{\mu_1}{J^{2/3}}(\delta_{ik}B_{jl} + B_{il}\delta_{jk} - \frac{2}{3}(B_{ij}\delta_{kl} + B_{kl}\delta_{ij}) + \frac{2}{3}\frac{B_{qq}}{3}\delta_{ij}\delta_{kl}) + K_1(2J-1)J\delta_{ij}\delta_{kl} \tag{3.36}$$

29

and

$$\boldsymbol{C}^{ani,0} = 4\psi_{,44}\boldsymbol{m} \otimes \boldsymbol{m} \otimes \boldsymbol{m} \otimes \boldsymbol{m} + 4\psi_{,66}\boldsymbol{m}' \otimes \boldsymbol{m}' \otimes \boldsymbol{m}' \otimes \boldsymbol{m}',$$

$$C^{ani,0}_{ijkl} = 4\psi_{,44}m_i m_j m_k m_l + 4\psi_{,66}m'_i m'_j m'_k m'_l, \tag{3.37}$$

with $\psi^{i=4,6}_{,ii}$ being the second derivative of the energy functions with respect to the pseudo-invariants

$$\psi^{i=4,6}_{,ii} = \partial_{I_i}\psi_{,i} = k_1(1 + 2k_2(I_i - 1)^2)\exp\big(k_2(I_i - 1)^2\big). \tag{3.38}$$

3.7 Active stress

The stress value equations in the last section only account for the passive stress generated by the material in response to some other sources of stress or deformation. The total stress is the summation of the active and passive stress

$$\boldsymbol{\tau} = \boldsymbol{\tau}_{act} + \bar{\boldsymbol{\tau}} = \boldsymbol{\tau}_{act} + \boldsymbol{\tau}_{pas}. \tag{3.39}$$

The active stress is a contraction stress caused by the tip cells trying to migrate towards the TAF source [51]. Extensive experiments have been conducted to study the active stress caused by the tip cells in migrations. Reinhart-King observed that the tip cell generates the most traction stress close to its walls and the least in its center [7, 6]. Edgar [5] believed that the traction's magnitude is maximum at the point of the tip cell and decreases exponentially with radius. Combining the results from the two researchers, an exponential function for the active stress value is developed here by changing the formula proposed by Edgar so the stress first increases around the tip cell's center point until it reaches the tip cell's walls, then it disperses exponentially (Figure 3.5). It was also said that the value of active stress would be maximum towards a tumour and decreases in other directions (Figure 3.6).
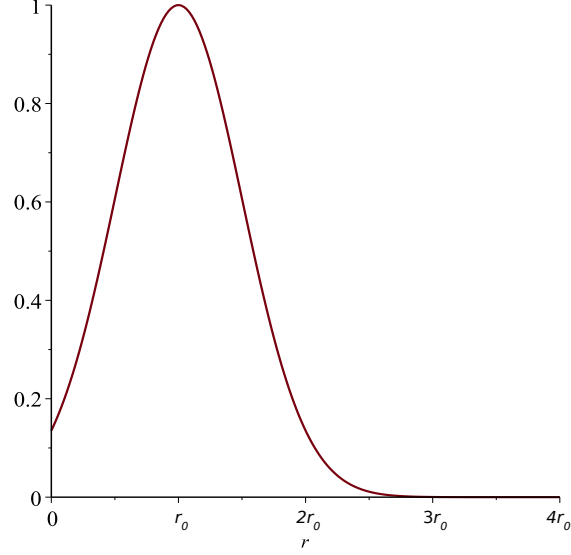
Figure 3.5: The term $e^{-b(\|\boldsymbol{r}\|-r_0)^2}$ in 3.41. It shows the intensity of the active stress with respect to distance. As seen in this figure, the magnitude of active stress increases until it reaches cell walls and then decreases exponentially. $b = 2 \times 10^6$ r_0 is assumed in this figure.

When the tip cell is at point $\boldsymbol{x}_s$, the active stress at any arbitrary point $\boldsymbol{x}$ can be calculated using the formulas (Figure 3.7),

$$\boldsymbol{r} = \| \boldsymbol{r} \| \, \hat{\boldsymbol{r}} = \boldsymbol{x}_s - \boldsymbol{x}, \tag{3.40}$$

$$\boldsymbol{\tau}_{act} = Jae^{-b(\|\boldsymbol{r}\|-r_0)^2} \left| \cos^N(\frac{\alpha}{2}) \right| \hat{\boldsymbol{r}} \otimes \hat{\boldsymbol{r}}, \tag{3.41}$$

$$\alpha = \psi - \theta. \tag{3.42}$$

The part $\hat{\boldsymbol{r}} \otimes \hat{\boldsymbol{r}}$ in 3.41 defines the direction of the stress tensor radial towards the tip cell. N , a, and b are parameters for adjusting the width, the magnitude, and the range of the stress field, respectively. In Figure 3.7, $\boldsymbol{e}^v$ is a unit vector towards the TAF source, and

31
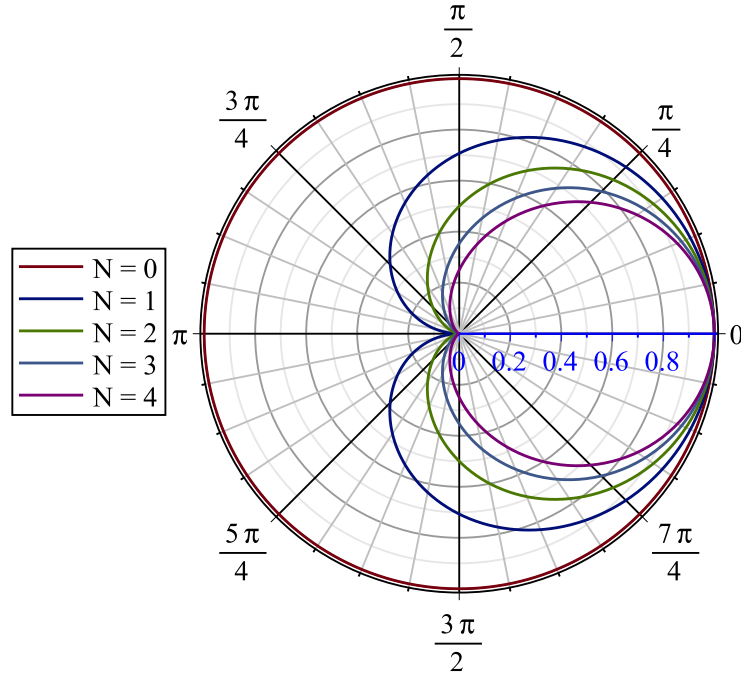
Figure 3.6: The term $\left|\cos^N\left(\frac{\alpha}{2}\right)\right|$ in the active stress formula. $\alpha = 0$ is the direction of the tip cell migration in the time step. As shown, increasing the value for N decreases the width of the stress field and makes it more concentrated towards the migration direction.

e_2^v is a unit vector showing the direction of the tip cell movement. This direction, e_2^v, is calculated by rotating e^v by θ. The value of θ is discussed in the next chapter.

The formula above is multiplied by a term to account for the effect of TAF level on the magnitude of active stress. The term is presented in [35, 30] and accounts for the decrease of chemotactic sensitivity with the increase of TAF concentration. It has a Michaelis-Menten rate law form as

$$\frac{1}{1 + \beta\xi},$$
(3.43)
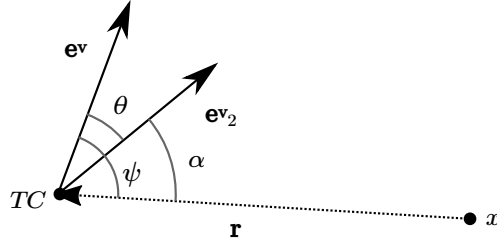
Figure 3.7: The tip cells generate active stress on the media. The location of the tip cell is represented by $\boldsymbol{TC}$ and the stress can be calculated at any point of $\boldsymbol{x}$. The unit vector $\boldsymbol{e}^v$ is directed towards the maximum TAF gradient and $\boldsymbol{e}_2^v$ shows the direction of the tip cell movement.

in which, ξ is the dimensionless TAF concentration and β is a dimensionless constant. The higher β is, the easier for the endothelial cells is to lose their chemotactic sensitivity. Other biomechanical variables can also affect the active stress. To see how active stress formulas are linked to the ECM density, please refer to [79].

The final value for active stress is shown below,

$$\boldsymbol{\tau}_{act} = \frac{1}{1 + \beta\xi} Jae^{-b(\|\boldsymbol{r}\| - r_0)^2} \left| \cos^N(\frac{\alpha}{2}) \right| \hat{\boldsymbol{r}} \otimes \hat{\boldsymbol{r}}. \tag{3.44}$$

3.8   Degradation function

The mechanical energy storage function for a multi-phase medium can be defined as [80]

$$\Psi(\boldsymbol{F}, \boldsymbol{A_m}, \boldsymbol{A_{m'}}, d) = g(d)\Psi_0^{ECM}(\boldsymbol{F}, \boldsymbol{A_m}, \boldsymbol{A_{m'}}) + (1 - g(d))\Psi_0^{EC}(\boldsymbol{F}, \boldsymbol{A_m}, \boldsymbol{A_{m'}}). \tag{3.45}$$

Here, $g(d)$ is the degradation function; it correlates the amount of phase transition to the change in mechanical energy storage. The equation above is an interpolation between the two values of energy for the ECM and the ECs so the value of $g(d)$ should be to be between
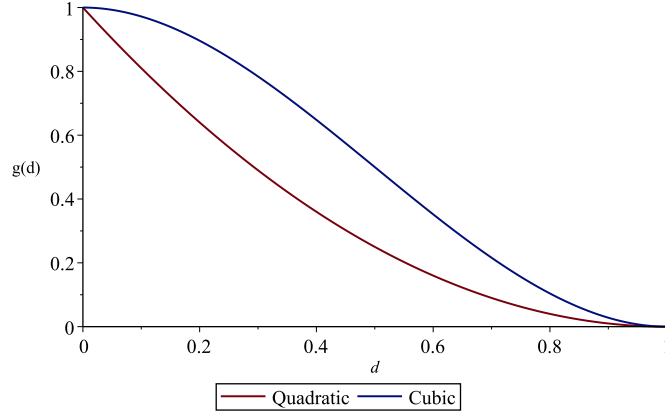
Figure 3.8: The quadratic and the cubic degradation functions for correlating the phase transition and mechanical energy storage.

0 and 1. All the conditions needed for $g(d)$ are

$$g'(d) \leq 0, \quad g(0) = 1, \quad g(1) = 0, \quad g'(1) = 0. \tag{3.46}$$

The most popular equations for the degradation function are the quadratic

$$g(d) = (1 - d)^2, \tag{3.47}$$

and the cubic

$$g(d) = m[(1 - d)^3 - (1 - d)^2] + 3(1 - d)^2 - 2(1 - d)^3 \tag{3.48}$$

equations (Figure 3.8). The cubic function is newer and it has been proposed in 2016 [81] by Borden. He proved that the cubic equation functions better in linear elastic problems. The quadratic equation is used for this research for its computational efficiency.

In the same way as the energy function, the active stress and the stiffness tensor are

interpolated as

$$\tau_{ij}^{pas} = F_{ik}\frac{\partial \Psi}{\partial F_{jk}} = F_{ik}\frac{\partial(g(d)\Psi_0^{ECM} + (1 - g(d))\Psi_0^{EC})}{\partial F_{jk}}$$
$$= g(d)\tau_{ij_0}^{ECM} + (1 - g(d))\tau_{ij_0}^{EC}, \tag{3.49}$$

$$C_{ijkl} = \frac{\partial \tau_{ij}}{\partial F_{km}}F_{lm} = \frac{\partial(g(d)\tau_{ij_0}^{ECM} + (1 - g(d))\tau_{ij_0}^{EC})}{\partial F_{km}}F_{lm}$$
$$= g(d)C_{ijkl_0}^{ECM} + (1 - g(d))C_{ijkl_0}^{EC}. \tag{3.50}$$

3.9 Derivation of the main two PDEs

In this section, using the minimization principle for the global power balance, the two main PDEs are derived.

First, an isotropic medium with no phase transition is considered. The energy storage function is

$$E(\boldsymbol{\varphi}) = \int_{\mathcal{B}} \Psi(\boldsymbol{F}, \boldsymbol{A_m}, \boldsymbol{A_{m'}})dV, \tag{3.51}$$

and the external work function is defined as

$$P(\boldsymbol{\varphi}) = \int_{\mathcal{B}} \rho_0 \bar{\boldsymbol{\gamma}} \cdot \boldsymbol{\varphi}dV + \int_{\partial\mathcal{B}} \bar{\boldsymbol{T}} \cdot \boldsymbol{\varphi}dA. \tag{3.52}$$

In the formula above, ρ_0 is the density, $\bar{\boldsymbol{\gamma}}$ is the prescribed body force and $\bar{\boldsymbol{T}}$ is the prescribed traction. All three are defined in the reference configuration. Also, note that Ψ is the free-energy function per unit volume in the reference configuration. The balance of the two formulas above are minimized below

$$\boldsymbol{\varphi} = \text{Arg}\left\{\inf_{\boldsymbol{\varphi}\in\mathcal{W}_\varphi} E(\boldsymbol{\varphi}) - P(\boldsymbol{\varphi})\right\}. \tag{3.53}$$

The Dirichlet-type boundary conditions below are assigned to the minimization equation

$$\mathcal{W}_\varphi = \{\boldsymbol{\varphi} \mid \boldsymbol{\varphi} \in H^1(\mathcal{B}), \boldsymbol{\varphi} = \bar{\boldsymbol{\varphi}} \text{ in } \bar{\boldsymbol{\varphi}} \in \partial\mathcal{B}_\varphi\}. \tag{3.54}$$

Solving equation 3.53 using the boundary conditions 3.54 the PDE below with the Neumann-type boundary conditions stated is derived

$$\nabla_{\boldsymbol{X}} \cdot \boldsymbol{P} + \rho_0 \bar{\boldsymbol{\gamma}} = \boldsymbol{0} \rightarrow \nabla \cdot \boldsymbol{P} + \rho_0 \bar{\boldsymbol{\gamma}} = \boldsymbol{0} \qquad \text{BC:} \quad \boldsymbol{P} \cdot \boldsymbol{N} = \bar{\boldsymbol{T}} \text{ on } \partial \mathcal{B}_t. \tag{3.55}$$

Now, the same approach as above, for a multi-phase medium would be used. The formulas derived here are the main formulas used in the biomechanical module. This time the energy storage function is defined using the free-energy function in 3.45 as below

$$E(\boldsymbol{\varphi}, d) = \int_{\mathcal{B}} \Psi(\boldsymbol{F}, \boldsymbol{A_m}, \boldsymbol{A_{m'}}, d) dV. \tag{3.56}$$

The external work function is the same as 3.52. Differentiating the energy storage function with respect to time results in rate of energy storage function

$$\mathcal{E}(\dot{\boldsymbol{\varphi}}, \dot{d}, \boldsymbol{\varphi}, d) = \int_{\mathcal{B}} (\boldsymbol{P} : \dot{\boldsymbol{F}} - f\dot{d}) dV. \tag{3.57}$$

In the formula above, $\boldsymbol{P}$ is the first Piola-Kirchhoff stress tensor

$$\boldsymbol{P} = \partial_{\boldsymbol{F}} \Psi(\boldsymbol{F}, \boldsymbol{A_m}, \boldsymbol{A_{m'}}, d) \tag{3.58}$$

and f is an energetic force conjugate to the crack phase-field

$$f = -\partial_d \Psi(\boldsymbol{F}, \boldsymbol{A_m}, \boldsymbol{A_{m'}}, d). \tag{3.59}$$

In the same way, by differentiating the external work function with respect to time, its rate is derived

$$\mathcal{P}(\dot{\boldsymbol{\varphi}}) = \int_{\mathcal{B}} \rho_0 \bar{\boldsymbol{\gamma}} \cdot \dot{\boldsymbol{\varphi}} dV + \int_{\partial \mathcal{B}} \bar{\boldsymbol{T}} \cdot \dot{\boldsymbol{\varphi}} dA. \tag{3.60}$$

Note that in the problem in this research, the terms in external work function are all zero because all the external effects are shown in active stress in the stress term in the energy storage function.

Another difference that the multi-phase energy formulas have with the formulas derived at the beginning of this section is the introduction of a new energy term. This term is called the transition energy function and is the amount of energy dissipated for the rupture of the ECM and the take over of the ruptured area with ECs

$$D_c(d) = \int_{\mathcal{B}} g_t \epsilon^2 \gamma(d, \nabla d) dV. \tag{3.61}$$

In the equation above, g_t is the critical energy needed to occupy the ECM space with the ECs and ϵ is the normalized ECM density discussed in the next chapter. Note that this parameter is always between zero and one so it reduces the energy needed for rupture. Differentiating this energy term with respect to time gets the transition dissipation function

$$D_c(\dot{d}) = \int_{\mathcal{B}} g_t \epsilon^2 (\delta_d \gamma(d, \nabla d)) \dot{d} dV, \tag{3.62}$$

$$\delta_d \gamma(d, \nabla d) = \frac{1}{l}(d - l^2 \Delta d). \tag{3.63}$$

Power balance equation is simply written by setting the summation of 3.57, 3.60, and 3.62 to zero

$$\Pi(\dot{\boldsymbol{\varphi}}, \dot{d}) = \mathcal{E}(\dot{\boldsymbol{\varphi}}, \dot{d}) + \mathcal{D}(\dot{d}) - \mathcal{P}(\dot{\boldsymbol{\varphi}}) = 0. \tag{3.64}$$

It can be written in the form of equation 3.53

$$\{\dot{\boldsymbol{\varphi}}, \dot{d}\} = \operatorname{Arg}\left\{ \inf_{\varphi \in \mathcal{W}_\varphi} \inf_{d \in \mathcal{W}_d} \Pi(\dot{\boldsymbol{\varphi}}, \dot{d}) \right\} \tag{3.65}$$

with $\mathcal{W}_\varphi$ and $\mathcal{W}_d$ defined as

$$\mathcal{W}_\varphi = \{\dot{\boldsymbol{\varphi}} \mid \dot{\boldsymbol{\varphi}} = \boldsymbol{0} \text{ on } \partial \mathcal{B}_\varphi\}, \quad \mathcal{W}_d = \{\dot{d} \mid \dot{d} = 0 \text{ on } \partial \mathcal{B}_d\}. \tag{3.66}$$

Solving the minimization problem above, the two PDEs below are derived

$$\nabla \cdot \boldsymbol{P} + \rho_0 \bar{\boldsymbol{\gamma}} = \boldsymbol{0} \qquad (f - g_t \epsilon^2 \delta_d \gamma) \dot{d} = 0. \tag{3.67}$$

The first PDE above can also be written as

$$J\nabla_{\boldsymbol{x}} \cdot (J^{-1}\boldsymbol{\tau}) + \rho_0\bar{\boldsymbol{\gamma}} = \boldsymbol{0} \tag{3.68}$$

with $\boldsymbol{\tau}$ denoting the Kirchhoff stress as defined in 3.31. As seen here, the first PDE is the same as the PDE seen for simple one-phase problems in 3.55. In the next section, we talk a little about the second PDE.

3.10   Phase change

The second PDE in 3.67 is discussed here, irreversibility of phase transition and mitosis will be added to the formulation.

First, using 3.63 and the second equation in 3.67, results in

$$f - \frac{g_t\epsilon^2}{l}(d - l^2\Delta d) = 0 \tag{3.69}$$

and considering 3.59 leads to

$$f = f^{ECM} - f^{EC} = 2(1-d)(\Psi_0^{\text{ECM}} - \Psi_0^{\text{EC}})$$

$$\rightarrow \begin{cases} f^{ECM} - (g_t^{ECM}/l)\epsilon^2(d - l^2\nabla d) = 0 \\ f^{EC} - (g_t^{EC}/l)\epsilon^2(d - l^2\nabla d) = 0. \end{cases} \tag{3.70}$$

In this formula, g_t^{ECM} is the critical energy needed for breaking the bonds in the ECM and g_t^{EC} is the energy needed for the formation of the ECs. Only the formula for the ECM is taken to account here to calculate the value for d. Renaming g_t^{ECM} to g_c and decomposing f^{ECM} to isotropic and anisotropic responses and solving 3.69 for each response results in

$$\Psi_0^{iso} = \Psi_{iso,0}^{\text{ECM}}, \quad \Psi_0^{ani} = \Psi_{ani,0}^{\text{ECM}}, \tag{3.71}$$

$$2(1-d)\frac{\Psi_0^{iso}}{g_c^{iso}\epsilon^2/l} = d - l^2\Delta d, \quad 2(1-d)\frac{\Psi_0^{ani}}{g_c^{ani}\epsilon^2/l} = d - l^2\Delta d. \tag{3.72}$$

38

Now, dimensionless mechanical transition driving functions for both responses can be defined as

$$\bar{\mathcal{H}}^{iso} = \frac{\Psi_0^{iso}}{g_c^{iso}\epsilon^2/l}, \quad \bar{\mathcal{H}}^{ani} = \frac{\Psi_0^{ani}}{g_c^{ani}\epsilon^2/l}. \tag{3.73}$$

The total mechanical transition driving function can be defined as the summation of the two so 3.69 would be transformed into

$$\bar{\mathcal{H}} = \bar{\mathcal{H}}^{iso} + \bar{\mathcal{H}}^{ani} \rightarrow \quad d - l^2\Delta d = (1-d)\bar{\mathcal{H}}. \tag{3.74}$$

Now the irreversibility condition would be added to the formula above with defining the history function $\bar{\mathcal{H}}$ as below

$$\mathcal{H} = \max_{s\in[0,t]}[\langle\bar{\mathcal{H}}(s) - 1\rangle]. \tag{3.75}$$

Here, $\langle\Box\rangle$ is the Macaulay brackets and is defined as $\langle\Box\rangle = (\Box + |\Box|)/2$. This function simply makes the value of $\mathcal{H}$ either be constant or increase in each time step (Figure 3.9). Also note that the minus one is there so that the phase transition would not start with any values of deformation. It would start when the Ψ_0 is more than the critical value g_c/l. Note that the formula above provides an energy-based failure criterion for mode I fracture. Mode I of fracture is the propagation of the crack because of tensile stress normal to plane of the crack. Stress-based failure criteria are provided in [61].

As mentioned in [48] a new term can be added to 3.69 to account for cell mitosis

$$f - \frac{g_c}{l}(d - l^2\Delta d) + \nu d(1-d)\langle\omega - \omega^t\rangle = 0. \tag{3.76}$$

In the formula above, ν is the proliferation constant for the endothelial cells and ω^t is the critical value of TAF concentration for the start of the proliferation. Also, ω is the normalized TAF concentration which is always between 0 and 1. Repeating everything done in this section, the formula below would be derived for irreversible phase transition
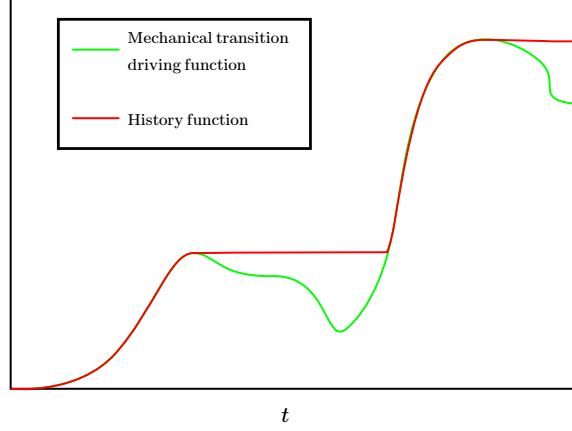
Figure 3.9: The relationship between the history function $\mathcal{H}$ and the total mechanical transition driving function $\bar{\mathcal{H}}$.

with mitosis

$$\underbrace{d - l^2\Delta d}_{\text{Geometric resistance}} = \underbrace{(1-d)\mathcal{H}}_{\text{Driving force}} + \underbrace{\nu_c d(1-d)\bar{\mathcal{G}}}_{\text{Proliferation}}, \quad \bar{\mathcal{G}} = \langle \omega - \omega^t \rangle, \quad \nu_c = \frac{\nu}{g_c/l}. \tag{3.77}$$

Note that the formula above and 3.74 are the main difference between the modelling framework in this research and the framework in other works on angiogenesis [30, 26, 48, 82]. In other research projects, there is no correlation between the biomechanical aspects of angiogenesis and ECs migration towards a tumour. Instead, they offer a term for chemotaxis which in this work is taken care of with the active stress term 3.39. They also model haptotaxis, related to ECM degradation, with a term in their phase-transition like PDE which is modelled here with ϵ in 3.73.

Refer to [82] to see sever al other terms like a term for natural degradation and a term for necrosis of the ECs.

40

3.11 Numerical implementation

In this section, the matrix form of formulas used in the computer code would be explained. To solve the two PDEs in 3.67, the staggered (as named in [59]) or the one-pass operator-splitting (as named in [3]) algorithm would be used. In this method, in every iteration, the two PDEs would be solved separately with the assumption of the other field variable staying constant. Here, first the displacement PDE would be solved, then the history function would be calculated over the domain followed by second PDE. This loop is repeated until convergence is met. The three steps are shown below.

$$
\begin{aligned}
&\rightarrow \text{(1)} \quad J\nabla_{\boldsymbol{x}} \cdot (J^{-1}\boldsymbol{\tau}) + \rho_0\bar{\boldsymbol{\gamma}} = \boldsymbol{0} \quad \& \quad \dot{d} = 0, \\
&\rightarrow \text{(2)} \quad \mathcal{H} = \max_{s\in[0,t]}[\langle\bar{\mathcal{H}}(s) - 1\rangle], \\
&\rightarrow \text{(3)} \quad d - l^2\Delta d = (1-d)\mathcal{H} \quad \& \quad \dot{\boldsymbol{\varphi}} = 0.
\end{aligned}
\tag{3.78}
$$

Discretizing the space of field variables and the reference domain $\mathcal{B}$ into subdomains $\partial\hat{\mathcal{B}}$ will result in the equation

$$
\boldsymbol{R} = \begin{bmatrix} \boldsymbol{R}_\varphi \\ \boldsymbol{R}_d \end{bmatrix} = \boldsymbol{0}.
\tag{3.79}
$$

In this equation, $\boldsymbol{R}$ is the residual vector and $\boldsymbol{R}_\varphi$ and $\boldsymbol{R}_d$ are the residual vectors for deformation and phase transition respectively. The formula above and the PDEs in 3.78 with the assumption of $\bar{\boldsymbol{\gamma}}$ and $\bar{\boldsymbol{T}}$ being equal to zero can be written in indicial form as follows

$$
\hat{R}_{\varphi,i}^a = \int_{\hat{\mathcal{B}}} \left(\frac{\partial\mathcal{N}^a}{\partial x_j}\hat{\tau}_{ij}\right)dV = \boldsymbol{0},
$$

$$
\hat{R}_d^a = \int_{\hat{\mathcal{B}}} \left(\mathcal{N}^a\Big(\hat{d} - (1-\hat{d})\hat{\mathcal{H}}\Big) + \frac{\partial\mathcal{N}^a}{\partial X_j}\hat{l}^2\frac{\partial\hat{d}}{\partial X_j}\right)dV = 0,
\tag{3.80}
$$

41

. Note that the sign $\hat{\square}$ shows that the quantities in the formulas above are associated with each element, for example, $\hat{\mathcal{H}}$ is the value of the history function in each element or $\hat{R}_{\varphi,i}^{a}$ is the value of the residual vector of the balance of linear momentum PDE in each element which needs to be assembled in the global residual vector. Also, the formulas are written for each node and each degree of freedom shown with the a superscript and i, j subscripts respectively. Here, $\hat{\tau}_{ij}$ is the Kirchhoff stress in each element and is calculated using 3.39. $\mathcal{N}^a$ is a scalar and contains the shape function for each node a.

The above nonlinear equations need to be linearized to be solved. The linearization process is done by using the first two terms of the Taylor series

$$\boldsymbol{R} + \frac{\partial \boldsymbol{R}}{\partial \boldsymbol{U}} \Delta \boldsymbol{U} = 0. \tag{3.81}$$

In this equation $\boldsymbol{U}$ contains the phase variables as

$$\boldsymbol{U} = \begin{bmatrix} \varphi^h \\ \boldsymbol{d}^h \end{bmatrix}. \tag{3.82}$$

There is a stiffness term also apparent in 3.81 which can be defined as follows

$$\boldsymbol{K} = \frac{\partial \boldsymbol{R}}{\partial \boldsymbol{U}} = \begin{bmatrix} \partial \boldsymbol{R}^\varphi / \partial \varphi & \boldsymbol{0} \\ \boldsymbol{0} & \partial \boldsymbol{R}^d / \partial \boldsymbol{d} \end{bmatrix} = \begin{bmatrix} \boldsymbol{K}_{\varphi\varphi} & \boldsymbol{0} \\ \boldsymbol{0} & \boldsymbol{K}_{dd} \end{bmatrix}. \tag{3.83}$$

The two stiffness matrices above for the nodes a, b and the degrees of freedom i, k in each element can be calculated with

$$
\begin{aligned}
\hat{K}_{\varphi\varphi,ik}^{ab} &= \int_{\hat{\mathcal{B}}} \left(\frac{\partial \mathcal{N}^a}{\partial x_j} \hat{C}_{ijkl} \frac{\partial \mathcal{N}^b}{\partial x_l} - \frac{\partial \mathcal{N}^a}{\partial x_k} \hat{\tau}_{ij} \frac{\partial \mathcal{N}^b}{\partial x_j} \right) dV, \\
\hat{K}_{dd,ik}^{ab} &= \int_{\hat{\mathcal{B}}} \left(\mathcal{N}^a \left(1 + \hat{\mathcal{H}} \right) \mathcal{N}^b + \frac{\partial \mathcal{N}^a}{\partial X_j} \hat{l}^2 \frac{\partial \mathcal{N}^a}{\partial X_j} \right) dV,
\end{aligned}
\tag{3.84}
$$

42

in indicial form. As a result, the equation 3.78 can be written in matrix form as

$$
\begin{aligned}
\rightarrow (1) \quad & \Delta\boldsymbol{\varphi}^h = -\boldsymbol{K}_{\varphi\varphi}^{-1}\boldsymbol{R}_\varphi, \\
\rightarrow (2) \quad & \mathcal{H} = \max_{s\in[0,t]}[\langle\bar{\mathcal{H}}(s) - 1\rangle], \\
\rightarrow (3) \quad & \Delta\boldsymbol{d}^h = -\boldsymbol{K}_{dd}^{-1}\boldsymbol{R}_d.
\end{aligned}
\tag{3.85}
$$

3.12   Conclusion

This chapter discussed the different components and the flow of the code. It explained the biomechanical module and the basic knowledge needed to comprehend it. All the equations presented here are borrowed from mentioned references except equations 3.44 and 3.61 which are modified to capture the physics of this problem better. At the end of running this part of the code, the stress and displacement fields and the propagation of the endothelial cells are calculated and will be passed on to the vascular network module.

Chapter 4

Biochemical & Vascular Network Modules

This chapter talks mainly about the two remaining modules in the solver. First, the biochemical module and then the vascular network module.

4.1   The biochemical module

This module is run once at the beginning of each time step. It uses the values of biochemical concentrations and the deformations from the previous time step to produce the new values for the concentrations and their rate of change. Because the PDEs in this module are both time and space dependent, both spatial and time discretization are required.

As seen in Figure 3.1A, this module first calculates the concentration of oxygen and MDE throughout the domain, then the values for TAF and the ECM level. The formulas

are based on mass conservation and Fick's laws, and the time integration is done using Crank-Nicolson method.

In this section, an approach like the one taken in the third chapter would be made. It will start with defining the field variables. Then the derivation of the formulas and their matrix form used in the solver will be presented.

4.1.1 Field variables

Four field variables are defined in this module representing the normalized values for concentrations that range between 1 and 0. Normalization is done by setting a maximum value for each of the four and then dividing the values for each concentration by that concentration. These phase variables are defined on the initial configuration, $\mathcal{B}$, and evolve with time. The four variables are normalized concentrations for oxygen, TAF, MDE, and the ECM's normalized density, denoted by $\xi_t(\boldsymbol{X})$, $\omega_t(\boldsymbol{X})$, $\mu_t(\boldsymbol{X})$, $\epsilon_t(\boldsymbol{X})$, respectively. All the four can be defined as

$$\Box_t(\boldsymbol{X}) : \begin{cases} \mathcal{B} \times \mathcal{T} \to [0,1], \\ (\boldsymbol{X}, t) \mapsto \Box = \Box(\boldsymbol{X}, t). \end{cases} \tag{4.1}$$

4.1.2 Fluxes, diffusion, and advection

Mass conservation equation and Fick's first law result in the advection-diffusion-reaction equation

$$\frac{\mathrm{d}c}{\mathrm{d}t} = -\nabla \cdot J_c + P_c - Q_c, \tag{4.2}$$

where c is the dimensionless normalized concentration. J_c is the diffusive flux of c. P_c and Q_c are the production and consumption rates, respectively. Using Fick's second law, the

diffusive flux can be defined as $J_c = -D_c \nabla c$ so the mass transfer formula becomes

$$\frac{\mathrm{d}c}{\mathrm{d}t} = D_c \Delta c + P_c - Q_c. \tag{4.3}$$

The material derivative of normalized concentration $(\mathrm{d}c)/(\mathrm{d}t)$ can be defined as

$$\frac{\mathrm{d}c}{\mathrm{d}t} = \frac{\partial c}{\partial t} + \frac{\partial c}{\partial \boldsymbol{x}} \cdot \frac{\partial \boldsymbol{x}}{\partial t}, \tag{4.4}$$

the second term here can be interpreted as the advection term when the flow is incompressible [83].

4.1.3 Reactions

The consumption rate in 4.3 is assumed to be only dependent on the species decay. The simplest decay model for a species is a linear decay with the reaction rate δ_c and only dependent on the substrates concentrations [84]. The decay process for Oxygen, TAF, and MDE can be depicted as

$$
\begin{aligned}
C &\xrightarrow{\delta_c} \\
Q_c &= \delta_c c.
\end{aligned} \tag{4.5}
$$

The decay of the ECM needs two substrates. It needs both ECM and MDE to decay so the formulas will be as

$$
\begin{aligned}
\mathrm{ECM} + \mathrm{MDE} &\xrightarrow{\delta_\epsilon} \\
Q_{\mathrm{ECM}} &= \delta_\epsilon \epsilon \mu,
\end{aligned} \tag{4.6}
$$

where δ_ϵ is the decay rate. The normalized concentrations of ECM and MDE are ϵ and μ respectively. Note that the formula only applies to the domain which tumour does not exist. The MDE does not degrade the tumour cells. To incorporate this into the formula,

46

a parameter $\bar{\rho}_{tum}$ can be defined which is equal to 0 where there is tumour and is equal to 1 anywhere else. Now 4.6 can be multiplied by $\bar{\rho}_{tum}$.

The easiest assumption for calculating the production rate is having an unlimited amount of substrates. This would result in a constant rate of production λ_c defined as

$$
\begin{gathered}
(\text{if cond}) \xrightarrow{\lambda_c} C, \\
P_c = \rho_{\text{cond}}\lambda_c,
\end{gathered}
\tag{4.7}
$$

which if a certain condition satisfies for each substrate in an element, then a constant rate is assumed or else the rate is zero. The first ρ_{cond} is ρ_{tum} which shows where the tumour is so ρ_{tum} is equal to 1 on the tumour and is equal to 0 everywhere else. The second ρ_{tum} is ρ_v, a parameter to show where vessels exist so it is equal to 1 on the capillaries and 0 on the ECM. Finally, ρ_t is equal to 1 in elements where tip cells exist and equal to 0 everywhere else. The three production rates are

$$
\begin{gathered}
P_\xi = P_{O_2} = \rho_v\lambda_\xi \\
P_\omega = P_{TAF} = \rho_{tum}\lambda_\omega \exp(-2\xi/\bar{\xi}) \\
P_\mu = P_{MDE} = \rho_{tum}\lambda_{\mu-c} + \rho_t\lambda_{\mu-v}.
\end{gathered}
\tag{4.8}
$$

4.1.4 Final PDEs

Setting the values for consumption and production rates for the four substrates in equation 4.3, results in the four equations

$$
\frac{\mathrm{d}\xi}{\mathrm{d}t} = \underbrace{\frac{\partial}{\partial \boldsymbol{X}} \cdot [D_\xi \frac{\partial \xi}{\partial \boldsymbol{X}}]}_{\text{Diffusion}} + \underbrace{\rho_v\lambda_\xi}_{\text{Production}} - \underbrace{\delta_\xi \xi}_{\text{Decay}},
\tag{4.9}
$$

$$
\frac{\mathrm{d}\omega}{\mathrm{d}t} = \frac{\partial}{\partial \boldsymbol{X}}[D_\omega \frac{\partial \omega}{\partial \boldsymbol{X}}] + \rho_{tum}\lambda_\omega \exp(-2\xi/\bar{\xi}) - \delta_\omega \omega,
\tag{4.10}
$$

47

$$\frac{\mathrm{d}\mu}{\mathrm{d}t} = \frac{\partial}{\partial \boldsymbol{X}}[D_\mu \frac{\partial \mu}{\partial \boldsymbol{X}}] + \rho_{tum}\lambda_{\mu-c} + \rho_t \lambda_{\mu-v} - \delta_\mu \mu, \tag{4.11}$$

$$\frac{\mathrm{d}\epsilon}{\mathrm{d}t} = -\delta_\epsilon \bar{\rho}_{tum}\epsilon\mu, \tag{4.12}$$

where ξ and ω are the values for the normalized concentration of oxygen and TAF respectively.

Equations 4.9 and 4.11 give the values for oxygen and ECM concentrations independent from the values for the other two substrates. So, to solve the system of PDEs, at first equations 4.9 and 4.11 are solved and then, the other two equations are solved.

4.1.5 Numerical implementation

The two main differences between the formulas derived here and the ones obtained in the previous chapter 3.67 are that the equations derived in this chapter are linear and time-dependent while the formulas in the other chapter where nonlinear and time independent. This time dependency requires the discretization of the PDEs both in time and space. Crank-Nicolson method [85] does the discretization in time. This method needs two steps to solve each of the PDEs. The two steps are

$$
\begin{aligned}
\rightarrow (1) \quad &\boldsymbol{d}_c^{n+1} = \left(\boldsymbol{A}^{n+1}\right)^{-1}\boldsymbol{R}^{n+1}, \\
\rightarrow (2) \quad &\dot{\boldsymbol{d}}_c^{n+1} = \frac{2}{\Delta t}\left(\boldsymbol{d}_c^{n+1} - \boldsymbol{d}_c^n\right) - \dot{\boldsymbol{d}}_c^n.
\end{aligned}
\tag{4.13}
$$

In the formulas above, the superscript in $\square^{n+1}$ shows the time step and $\dot{\square}$ shows the derivative with respect to time. The vector $\boldsymbol{d}_c$ contains the value of normalized concentration for each ξ, ω, μ, and ϵ so in a four-node element is a 4×1 vector. The time step size is

defined with Δt. The matrix $\boldsymbol{A}^{n+1}$ and the vector $\boldsymbol{R}^{n+1}$ are defined as

$$\boldsymbol{A}^{n+1} = \boldsymbol{C} + \frac{\Delta t}{2}\boldsymbol{K}_t^{n+1}, \tag{4.14}$$

$$\boldsymbol{R}^{n+1} = \frac{\Delta t}{2}\boldsymbol{f}^{n+1} + \frac{\Delta t}{2}\left(\boldsymbol{C}\dot{\boldsymbol{d}}_c^n\right) + \boldsymbol{C}\boldsymbol{d}_c^n. \tag{4.15}$$

In the two formulas above, the definition of $\boldsymbol{K}_t^{n+1}$ and $\boldsymbol{f}^{m^{n+1}}$ are dependent on the substrate as shown below.

$$
\begin{aligned}
\text{if material} = \text{ECM} \quad &\to \quad \boldsymbol{K}_t^{n+1} = \boldsymbol{K}_t^{m^{n+1}} = \boldsymbol{K}_{\text{adv}}^{n+1} + \boldsymbol{U}^{m^{n+1}}, \\
&\to \quad \boldsymbol{f}^{m^{n+1}} = \boldsymbol{0}. \\
\text{other} \quad &\to \quad \boldsymbol{K}_t^{n+1} = \boldsymbol{K}_t^{c^{n+1}} = \boldsymbol{K}_{\text{adv}}^{n+1} + \boldsymbol{U} + \boldsymbol{K}, \\
&\to \quad \boldsymbol{f}^{c^{n+1}} = \boldsymbol{P}_c^{n+1}.
\end{aligned}
\tag{4.16}
$$

Matrix $\boldsymbol{C}$ in equation 4.15 and the five new matrices above are defined as

$$
\begin{aligned}
\hat{K}_{\text{adv}}^{ab} &= \int_{\hat{\mathcal{B}}}\left(\mathcal{N}^a v_i D_{il}\frac{\partial \mathcal{N}^b}{\partial X_l}\right)dV, \qquad \hat{K}^{ab} = \int_{\hat{\mathcal{B}}}\left(\frac{\partial \mathcal{N}^a}{\partial X_i}D_c\frac{\partial \mathcal{N}^b}{\partial X_i}\right)dV, \\
\hat{C}^{ab} &= \int_{\hat{\mathcal{B}}}\left(\mathcal{N}^a\mathcal{N}^b\right)dV, \qquad \hat{P}^a = \int_{\hat{\mathcal{B}}}\left(\mathcal{N}^a\hat{P}\right)dV, \\
\hat{U}^{m^{ab}} &= \int_{\hat{\mathcal{B}}}\left(\mathcal{N}^a\hat{\mu}\mathcal{N}^b\right)dV, \qquad \hat{U}^{ab} = \delta_c\hat{C}^{ab}.
\end{aligned}
\tag{4.17}
$$

The notation here is the same as the one used in chapter 3.11. Note that $\hat{P}$ is calculated from 4.8. Matrix $\boldsymbol{D}$ is defined in the same fashion as the deformation gradient in 3.5 and $\boldsymbol{v}$ is the velocity vector,

$$
\begin{aligned}
\boldsymbol{D} &= \frac{\mathrm{d}\boldsymbol{X}}{\mathrm{d}\boldsymbol{\varphi}} = \frac{\mathrm{d}\boldsymbol{X}}{\mathrm{d}\boldsymbol{x}}, \qquad D_{il} = \frac{\partial X_i}{\partial x_l}, \\
\boldsymbol{v} &= \frac{\mathrm{d}v}{\mathrm{d}t}, \qquad v_i = \frac{\partial x_i}{\partial t}.
\end{aligned}
\tag{4.18}
$$
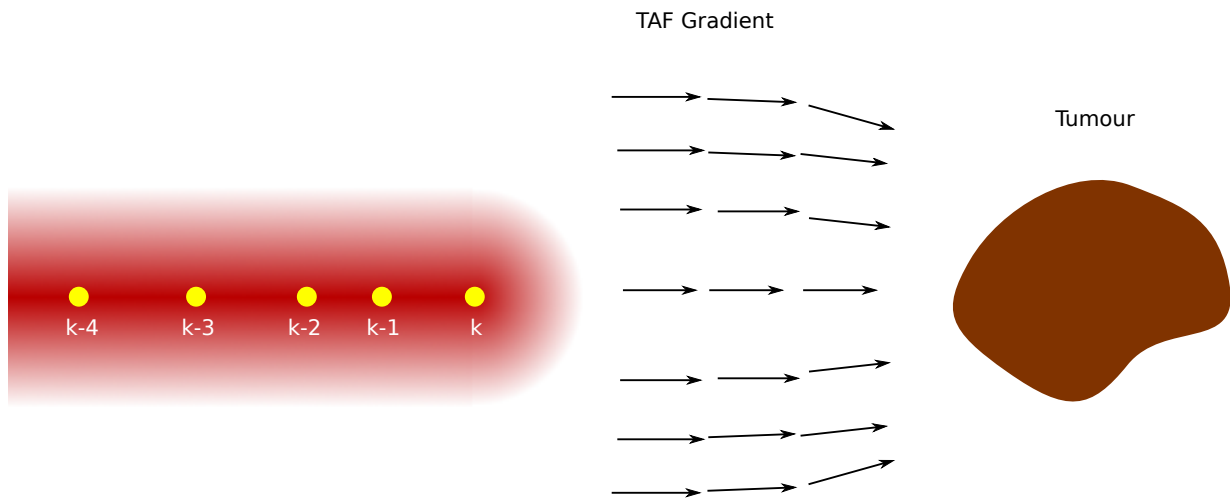
Figure 4.1: A branch in angiogenesis. Except tumour location, all the data presented here are all the biochemical and biomechanical data needed for vascular network module.

4.2 The vascular network module

The last module in the solver is the vascular network module. In contrast to the other modules, this module is not about solving any PDEs and the most computational intensive calculation done in it is solving a one-dimensional nonlinear equation using the Newton-Raphson method. This module is run at the end of each time step and calculates the force at each tip cell, checks if there is a need for the movement of the tip cell, and finds its new location. All these are discussed in the first subsection. The second subsection presents branching formulations.

4.2.1 Update tip cells

This sub-module first calculates the magnitude of force at each of the tip cells linearly, based on whether the tip cell is on the rising phase or not (all the tip cells $k-4, k-3, ..., k$
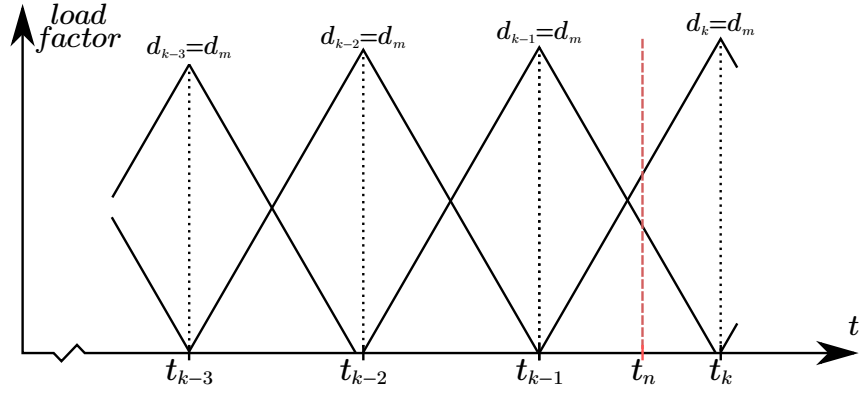
Figure 4.2: Loading on different locations of the tip cell throughout the time. The load factor is a dimensionless parameter which will be multiplied to equation 3.44 in each time step to calculate the active stress. This figure shows that in the vicinity of $t = t_n$ the load factor for the tip cell $k-1$ is decreasing and increasing for tip cell k. Figure 4.1 corresponds to $t \in [t_k, t_{k+1}]$.

in Figure 4.1). When a new tip cell is formed, it is defined in the rising phase, and the previous tip cell on the same branch will be marked in decline phase. In problems here only the last two of the tip cells have a value other than zero. The load factor change with time for Figure 4.1 is depicted in Figure 4.2. The last two tip cells can be interpreted as a stretched tip cell as seen in [7, 6].

Then the last tip cells in each of the branches (tip cell k) is checked to see if the phase transition parameter $d(\boldsymbol{r})$ in each of them exceeds d_{max}, if it does, the search for the new tip cell in that branch will be started (tip cell $k + 1$).

The new tip cell is found in the direction of the e_2^v (Figure 4.3A) as defined in Figure

51
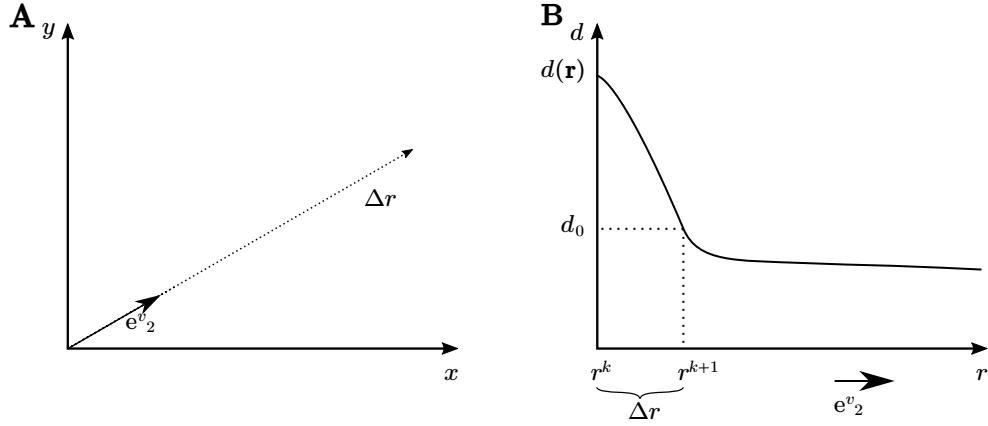
Figure 4.3: A: The direction of the next tip cell. B: The evolution of the transition parameter in the e_2^v direction from the point r^k and the distance (Δr) of the next point r^{k+1} from the point r^k.

3.7. The formulas for calculating e_2^v are

$$e^v = \frac{\nabla\omega(r^k)}{\|\,\nabla\omega(r^k)\,\|}, \tag{4.19}$$

$$e_2^v = A(\theta)e^v, \tag{4.20}$$

where r^k is the location of the tip cell k and $A(\theta)$ is the transformation function rotating e^v by θ. The angle θ is calculated using the normal distribution to account for the stochastic movement of the tip cell.

When the direction of the next tip cell is found, its location is calculated as (Figure 4.3B)

$$\Delta d_v = \nabla d(r) \cdot e_2^v,$$
$$\Delta r = \frac{d(r) - d_0}{\Delta d_v}, \tag{4.21}$$
$$r^{k+1} = r^k + e_2^v \Delta r.$$

In the formulas above d_0 is the initial transition value at the tip cell $k + 1$.

4.2.2 Branching

Most of the branching models in the literature use probability functions in each time step on unbranched areas of the newly formed vessel to see if branching happens or not. In these models, a random number for each of the previous tip cell locations using the uniform distribution would be generated. These numbers are between 0 and 1. The probability of branching is B, and if the random number is smaller than B, then branching occurs in the selected previous tip cell.

The same is implemented in this solver for branching. If the steps above indicates that branching is required, the solver searches for the next tip cell that originates from the node that caused the branching. The equations 4.20 and 4.21 would be used to find the new tip cell with a small difference. Now, θ_2 would be used instead of θ which is defined as

$$\theta_2 = \theta + \theta_0 \tag{4.22}$$

with θ_0 being a constant.

Here, B is assumed constant but as referred in [5, 30, 26] it can be a function of TAF concentration, the age of the vessels, the distance of the point from a tumour, or the biofluidic parameters like wall shear stress in the capillaries.

4.3 Conclusion

This chapter first discussed the biochemical module and presented a set of four partial differential equations to model the concentration of each substrate in the domain. This module uses the displacement field generated by the biomechanical module as an input. The chapter then discusses the vascular network module which is the most innovative part

of this chapter. This module uses the phase transition data to find the next tip cell location in each time step and check for branching. The components discussed in this chapter and the one before it complete the engine needed for this new approach to analyze angiogenesis.

Chapter 5

Results and Discussion

The previous chapters discussed the theoretical aspects and the numerical implementations. This chapter covers the specifics about the model and the results. The specifics include the values for parameters, the geometry, and the initial and boundary conditions. The results are generated for a certain problem, and are discussed in the last section of the chapter. The final thoughts are presented in the next chapter.

5.1 Parameters

Different parameters are investigated through this model. Just as the modules, they can be classified as biochemical, biomechanical, and vascular parameters and they are represented by the three following tables. Table 5.1 contains the biochemical parameters as reported in [1]. Note that the parameterless entries in the table are the value used to make the concentration values, $\omega, \xi, \mu, \epsilon$, dimensionless. Also, note that the oxygen uptake is different in the tumour and the host.

Table 5.1: Biochemical parameters [1]

Substrate	Description	Parameter	Value	Unit
TAF	production rate	λ_ω	9.996	d^{-1}
	decay rate	δ_ω	8.64×10^{-2}	d^{-1}
	diffusion coefficient	D_ω	9.99×10^{-1}	$\mathrm{mm^2\ d}^{-1}$
	max concentration	$-$	1×10^{-8}	$\mathrm{g\ cm}^{-3}$
Oxygen	production rate	λ_ξ	0.288	d^{-1}
	uptake by the host	δ_ξ	1.38×10^{-3}	d^{-1}
	uptake by the tumour	δ_ξ	1.725×10^{-2}	d^{-1}
	diffusion coefficient	D_ξ	3.455×10^{-3}	$\mathrm{mm^2\ d}^{-1}$
	TAF related parameter	ξ	0.6	$-$
MDE	tumour's production rate	$\lambda_{\mu-c}$	4.32×10^{-2}	d^{-1}
	TC's production rate	$\lambda_{\mu-v}$	8.64×10^{-3}	d^{-1}
	decay rate	δ_μ	1.0368×10^{2}	d^{-1}
	diffusion coefficient	D_μ	7.344×10^{-1}	$\mathrm{mm^2\ d}^{-1}$
	max concentration	$-$	1×10^{-13}	$\mathrm{Mol\ cm}^{-3}$
ECM	degradation rate	δ_ϵ	6.912	d^{-1}
	reference density	$-$	0.1	$\mathrm{g\ cm}^{-3}$

Table 5.2 contains parameters and their values for the biomechanical module. The values for the mechanical properties of both the ECM and the ECs are derived from [51, 3, 86]. As seen in the table, the anisotropic parameters related to the endothelial cells are zero because it is assumed that it takes some time for the network of collagen fibres to

Table 5.2: Biomechanical parameters [2, 3, 4, 5, 6, 7]

Category	Description	Parameter	Value	Unit
EC	shear modulus	μ_1^{EC}	5.0×10^{-3}	MPa
	penalty term	K_1^{EC}	5.0	MPa
	stress-like material parameter	k_1^{EC}	0	MPa
	dimensionless parameter	k_2^{EC}	0	–
ECM	shear modulus	μ_1^{ECM}	1.0×10^{-2}	MPa
	penalty term	K_1^{ECM}	10	MPa
	stress-like material parameter	k_1^{ECM}	2.0×10^{-2}	MPa
	dimensionless parameter	k_2^{ECM}	1.0	–
Phase transition	length-scale parameter	l	2.0×10^{-2}	mm
	critical transition energy	g_c^{iso}	5.0×10^{-4}	MPa mm
	critical transition energy	g_c^{ani}	1.5×10^{-3}	MPa mm
Active stress	magnitude	a	0.200	MPa
	range	b	1.4×10^4	mm^{-2}
	width	N	2	–
	EC's radius	r_0	1.4×10^{-2}	mm
	Michaelis-Menten coefficient	β	0.6	–

form in the newly-constructed capillaries. The phase transition parameters are taken from [2, 3, 4]. Finally, stress-related equation was developed based on [5] and calibrated with experimental data provided by [6, 7].

To our knowledge, no parameters required for the vascular network module are available

in the literature. To find the value of parameters reported in 5.3 required for our model, we ran our model several times (trial and error) using the examples reported in [26] until the same results are reached.

Table 5.3: Vascular parameters

Sub-module	Description	Parameter	Value	Unit
Tip cell migration	production rate	$d_{\max}$	0.20	–
	decay rate	d_0	0.15	–
	mean for θ in 4.20	–	0.0	–
	standard deviation for θ in 4.20	–	$\pi/18$	–
Branching	branching probability	B_0	0.1	–
	new sprout angle	θ_0	$\pi/2$	–

5.2   Initial and boundary conditions

There are six partial differential equations in this analysis. Boundary and initial conditions are defined for each of the PDEs. Two types of boundary conditions exist in this problem. Neumann boundary conditions which specify the value of the normal derivative of the functions are already included in the formulations (3.26) but will be included here for convenience.

$$\bar{\boldsymbol{T}} = \boldsymbol{0} \quad , \quad \nabla d \cdot \boldsymbol{N} = 0 \quad \text{on } \partial\mathcal{B},$$

$$\boldsymbol{q}_\omega = \boldsymbol{q}_\xi = \boldsymbol{q}_\mu = \boldsymbol{q}_\epsilon = \boldsymbol{0} \quad \text{on } \partial\mathcal{B}. \tag{5.1}$$

The values for $\boldsymbol{q}_\square$ show the flux of $\square$ on the boundaries.

Dirichlet boundary condition is only defined for the first PDE, the deformations PDE. This type of boundary condition defines the value of the function on the boundaries. Here, the deformation is set to be zero in the normal direction to the boundary.

The initial values ($t = 0$) for the deformation PDE are the deformation being equal to zero throughout the domain. So the system is at rest mechanically at the beginning. The phase transition is set to zero over the domain, so the entire domain is filled with the extracellular matrix at the beginning. The nodes with the parent vessel on them will have $\mathcal{H} = 5.0$. Equation 3.74 calculates the value for the phase-field parameter using the initial value for $\mathcal{H}$ in the first time step so by the end of the initial time step the location of the parent vessel is set.

The rate of change for all the biochemical concentrations is set to zero at the initial time. The concentrations for MDE and TAF are also supposed to be zero throughout the domain at time zero. The normalized oxygen concentration is equal to one throughout the domain except inside the tumour where it is equal to zero to account for the hypoxia (as an extreme case) inside the tumour initiating the tumour-induced angiogenesis. The initial normalized ECM density is equal to one.

5.3   Geometry

All the problems solved in this project are defined in the two-dimensional space. Bilinear quadrilateral elements are used in the analysis with the plane strain assumption. The domain is a square with the dimension of 0.4 mm. The geometry is depicted in Figure 5.1. The result of the Dirichlet boundary conditions explained in the previous section is simple supports constraining the movement of the boundaries in their normal directions, so the top and bottom boundaries constrain the movement in y-direction and the left and right
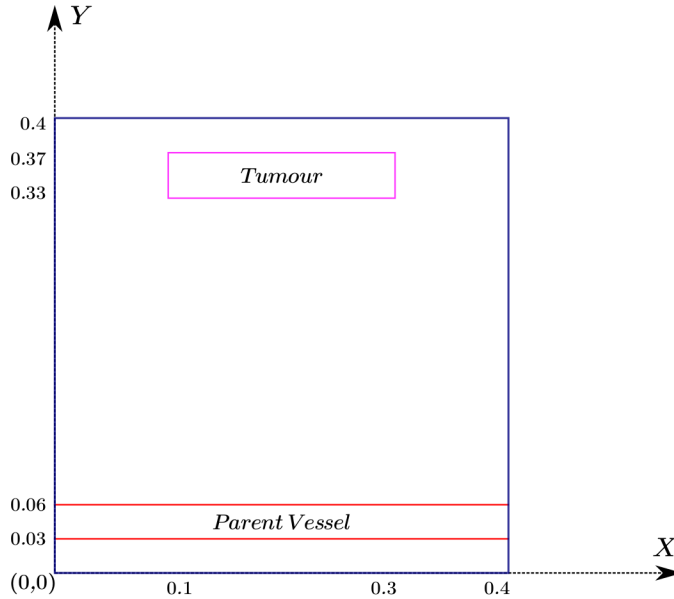
Figure 5.1: The general geometry of the examples solved here. The parent vessel is generated in the first time step. Dimensions in the figure are in mm.

boundaries constrain the movement in x-direction. According to [2], the maximum value for the element size is half of the value of l. So, the element size $h = 0.01$ is used here.

The tip cell is at $(0.2, 0.08)$ initially for the first, second, and the last examples and it later moves towards the tumour in the next time steps using the vascular network module.

5.4 Models and discussion

This section contains four models. They are different in the vascular network module and initial conditions. The first model has no stochastic movement, θ in 4.20 is equal to zero. Next models get more detailed with the guided random walk, more initial tip cells, and branching, each added in the second, third, and fourth model, respectively. The differences

between the four models are demonstrated in Table 5.4.

Table 5.4: Differences between the four models

Model	Stochastic Movement	Number of tip cells	Branching
I	✗	1	✗
II	✓	1	✗
III	✓	2	✗
IV	✓	1	✓

5.4.1 Model I: No stochastic movement

In this model, the normal distribution which produces the values for θ in 4.20 is turned off. Figure 5.2 shows the resulting phase transition at four different time steps. The parent vessel and the tumour location is the same as the one depicted in 5.1. The maroon area is the location of a tumour. The white dots show the path of the movement of the tip cell. The first tip cell is on the parent vessel wall. The tip cell moves upward towards the tumour, and a branch starts forming behind it. As seen in the figure, the tip cell has moved in a straight line because all the TAF gradient vectors between the initial tip cell's location and the tumour are collinear. That is because of the symmetry in the problem. The bar on the right side defines the value for the phase-field parameter. As seen here, the parameter is higher on the parent vessel compared to the newly created capillary.

The shape of the parent blood vessel at the junction is the same shape seen in [51]. Note that the transition parameter in the figure is shown in the initial configuration, so the deformations are not shown here. As seen in the figure, the first jump for the tip cell
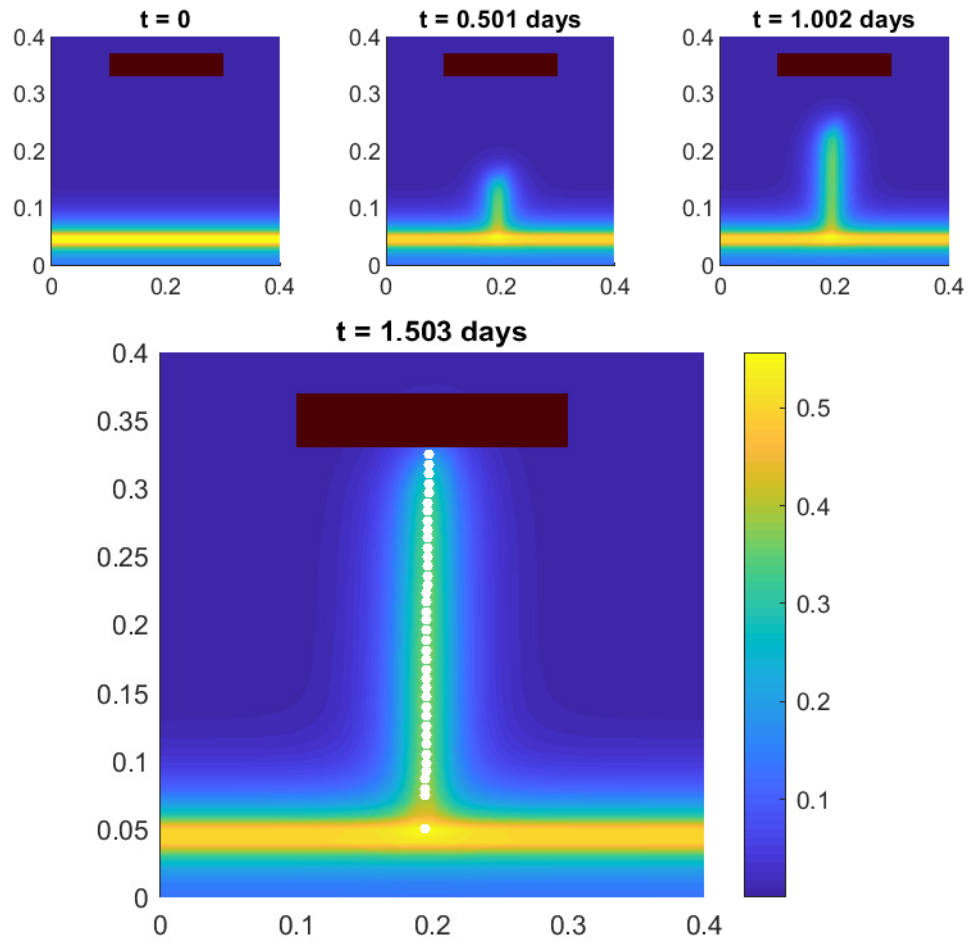
Figure 5.2: The growth of one capillary towards a tumour for model I. This figure shows the phase-field parameter at the end of the analysis. The maroon rectangle is a tumour. The white dots show the tip cell path throughout the time which the lowest is the location of the tip cell at time zero. The bar shows the phase-field parameter, zero is for extracellular matrix and one is for endothelial cells.
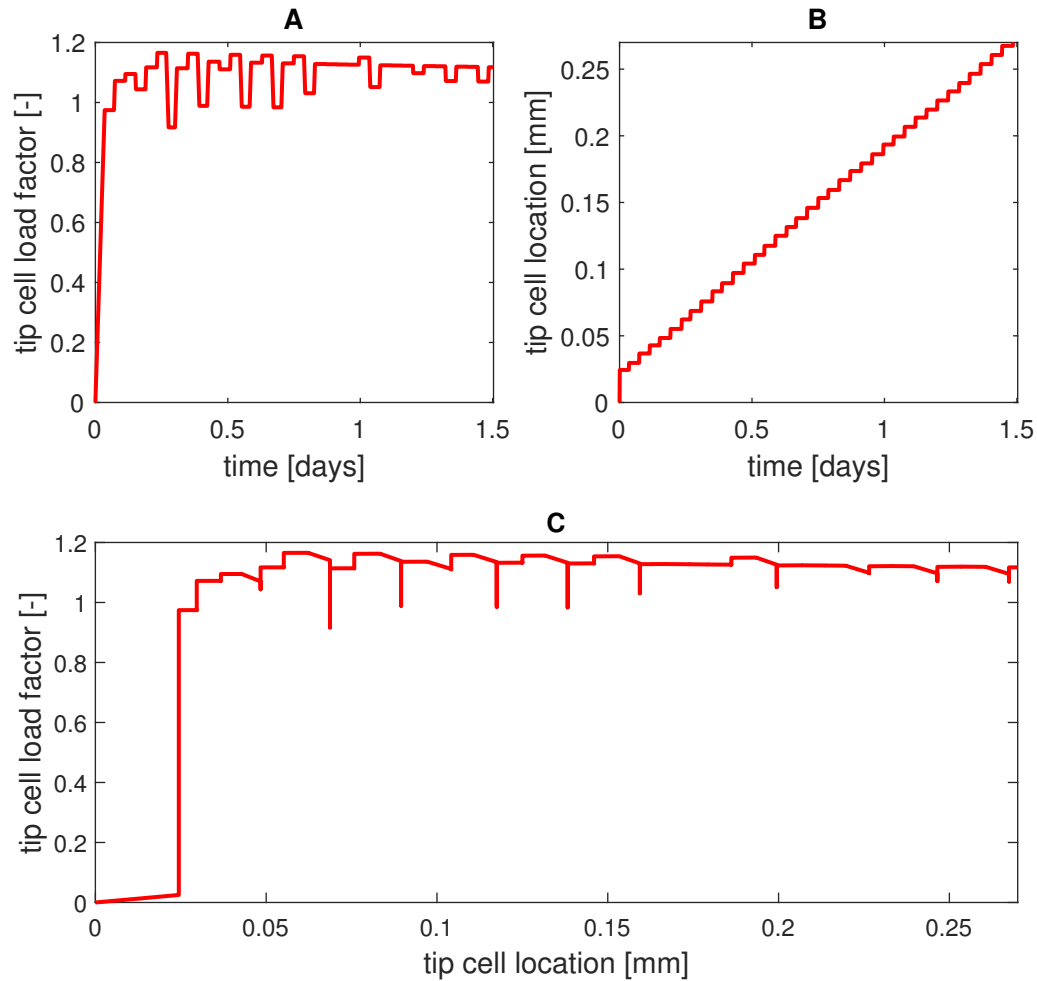
Figure 5.3: Tip cell load factor and tip cell location evolution throughout the analysis time for model I.

is longer than other jumps; it is because the tip cell jumped at $d = 0.50$ at this point while it jumps at $d = d_{max} = 0.20$ at other points. The initial jump can be reduced by closing the values for d_{max} and d_0 or reducing the value for l and the mesh size.

Tip cell load factor defined in Figure 5.3A is the sum of the loading factors depicted in Figure 4.2. As seen in 5.3A, the load factor increases until it reaches 1, meaning that

maximum load is $a = 200$ kPa, the value defined in Table 5.2, then stays roughly constant until the end of analysis in the branch. Figure 5.3B shows the closest location of the tip cell to the tumour, tip cell k in Figure 4.1, with respect to time. The jumps discussed in Figure 5.2 are seen here too. As discussed before, the first jump which happens in the first time step is longer and can be seen here at $t \approx 0$. The time difference between the jumps is close to equal which is because the total time is short and the TAF level is low for the term $1/(1 + \beta\xi)$ to have any major effects on the active stress produced by 3.44. Figure 5.3C correlates the last tip cell location and the total tip cell load factor. The jags seen in this plot are similar to those reported in [61]. The aberrations seen in Figure 5.3A and 5.3C can be diminished by reducing the time step size or the element size. The verification of this model in presented in the next section.

5.4.2   Model II: Stochastic movement of the tip cell

The second model is the same as the first model with the normal distribution turned on allowing a directed random movement of the tip cells. The normal distribution parameters are chosen so that the end result of the solver are morphologically consistent with the results from the earlier analysis done by others.

Figure 5.4 shows the formation of the capillary towards a tumour. Now, the cell did not go in a straight line to reach the tumour. It also went a little slower than in model I which is intuitive because the path it is taking the model is a little longer.

Figure 5.5 shows the same information shown in Figure 5.3. Here, the fluctuations in tip cell load factor are a little larger. This is because the local geometry at the different tip cell locations constantly changes because of the stochastic movement of the tip cell. This change in the geometry can make the extracellular matrix less prone to crack at some

64

Figure 5.4: The growth of one capillary towards a tumour for model II. This model is different from the first model in using a normal distribution to find the tip cell location.

points or more prone at some other points.
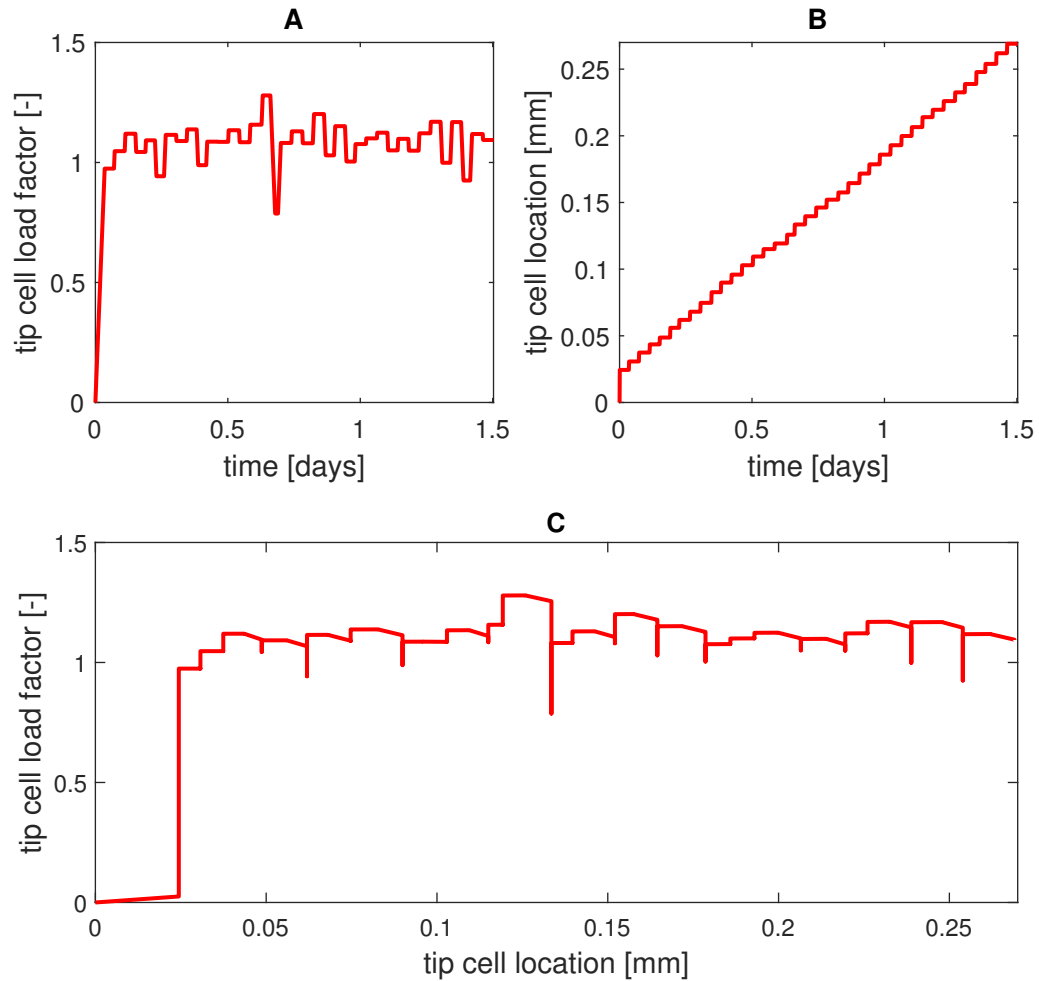
Figure 5.5: Tip cell load factor and tip cell location evolution throughout the analysis time for model II.

5.4.3 Model III: Two tip cells

Unlike previous models, this model has two tip cells initially at the same y-coordinate as the one in the previous models and the x-coordinates of 0.133 mm and 0.267 mm, respectively. The tip cell locations are not shown in Figure 5.6 to better see the phase

transition. As seen in the figure the "straighter" branch, the branch on the left, reached the tumour slightly sooner than the other branch which is intuitive.

Figure 5.7A shows the tip cell load factor for the branches and same as the previous models the two branches have fluctuations. Figure 5.7B confirms that the left branch is slightly faster than the right branch.

Comparing this model with model II, it can be inferred that the speed of the endothelial cells migration is about the same in the two models. As mentioned in chapter three, equation 3.41, $e^{-b(\|r\|-r_0)^2}$ defines the magnitude of the active stress exerted by the tip cells on the extracellular matrix. With the parameters defined in Table 5.2, the effective range of the active stress is 27 μm. The effective range is defined here as the range that active stress is more than 10% of its maximum value. It is intuitive that to have two active stress fields affecting each other, their distance, the distance of their centers, should be at most summation of the two effective ranges. The distance of the two tip cells in this model is 134 μm which is more than twice the effective range of the tip cells, 54 μm, so the two tip cells effect on each other is negligible. The distance between the two tip cells is why model I and model II tip cells have the same speed.

Decreasing the distance between the two tip cells will result in the two stress fields affecting resulting in tip cells migrating faster. This phenomenon also occurs in the next model, as at some points, the tip cells for different branches are closer to each other than the effective range. The effect of this will be discussed in the next subsection.

5.4.4 Model IV: Stochastic movement with branching

This model is the same as the second model, but the branching engine is turned on in this model. Because of the random nature of branching, some constraints are set in the branch-
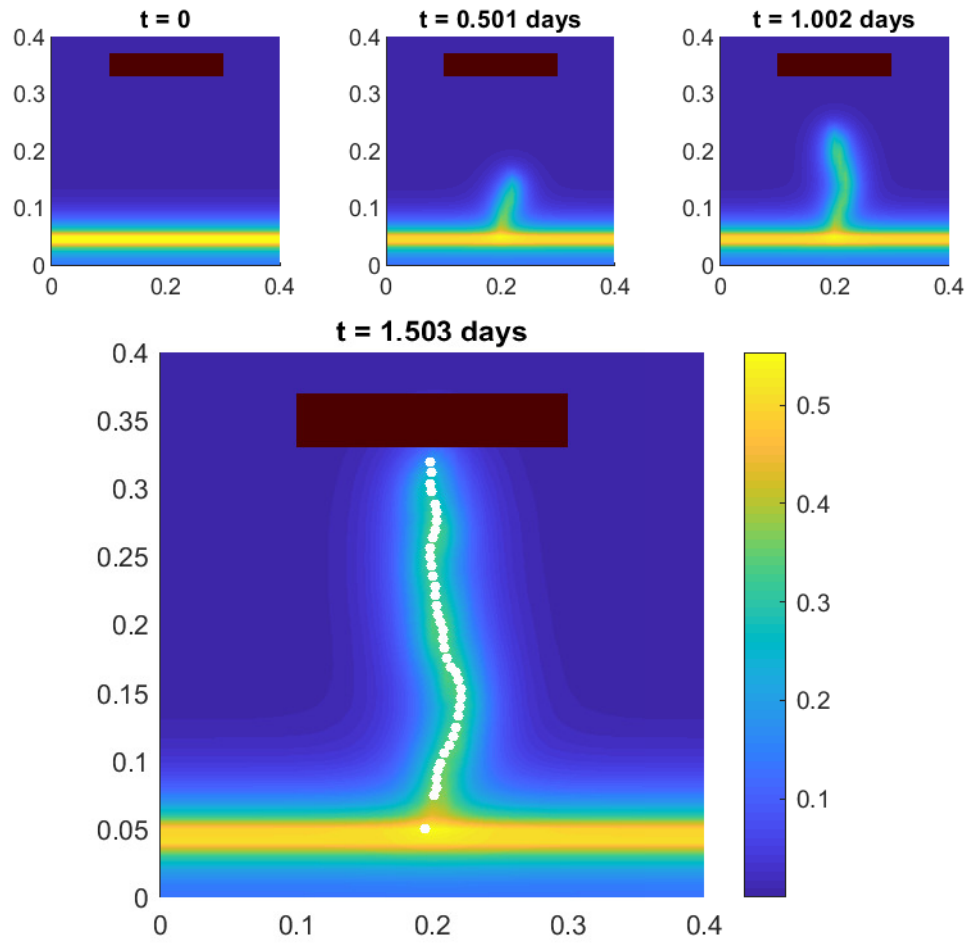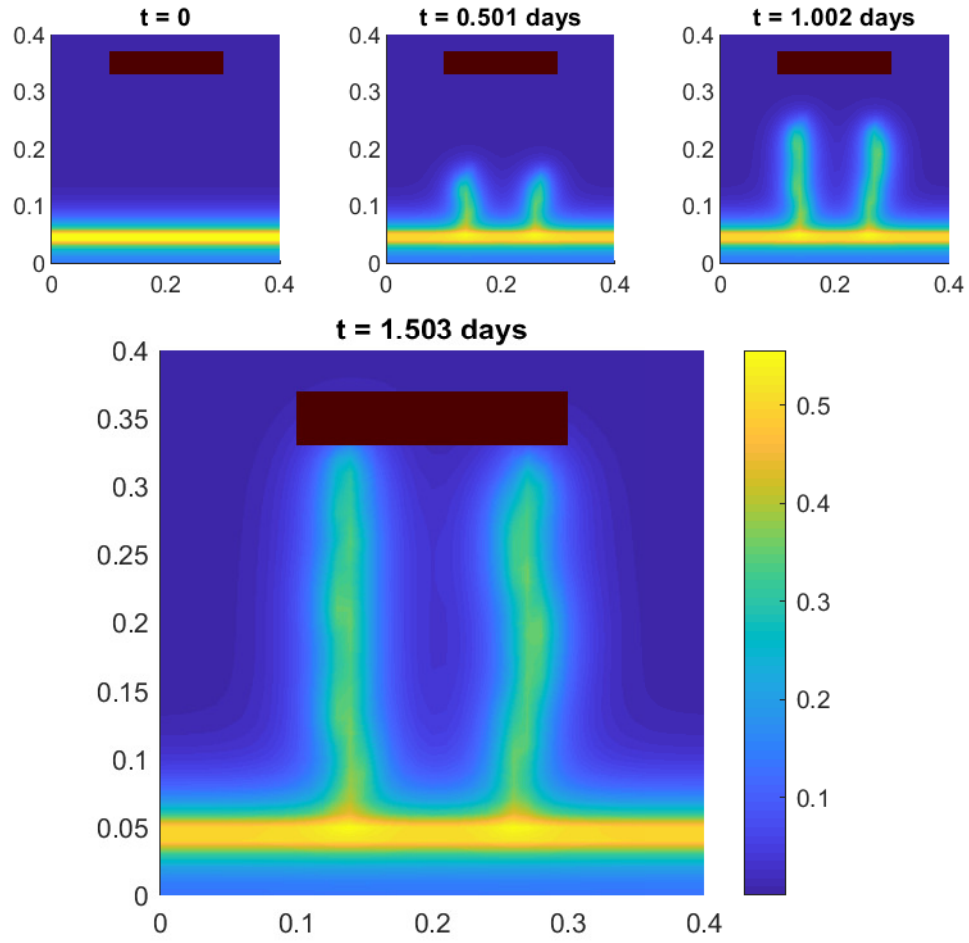
Figure 5.6: The growth of one capillary towards a tumour for model III. This model is different from the second model by having two tip cells initially.

ing engine to improve the model's operation. Similar approach was applied in literature as seen in [64]. First, no branching would happen in $y < 0.12$ mm. When a branch appears in a location, no more branches can occur in the next eight tip cell locations. Moreover,
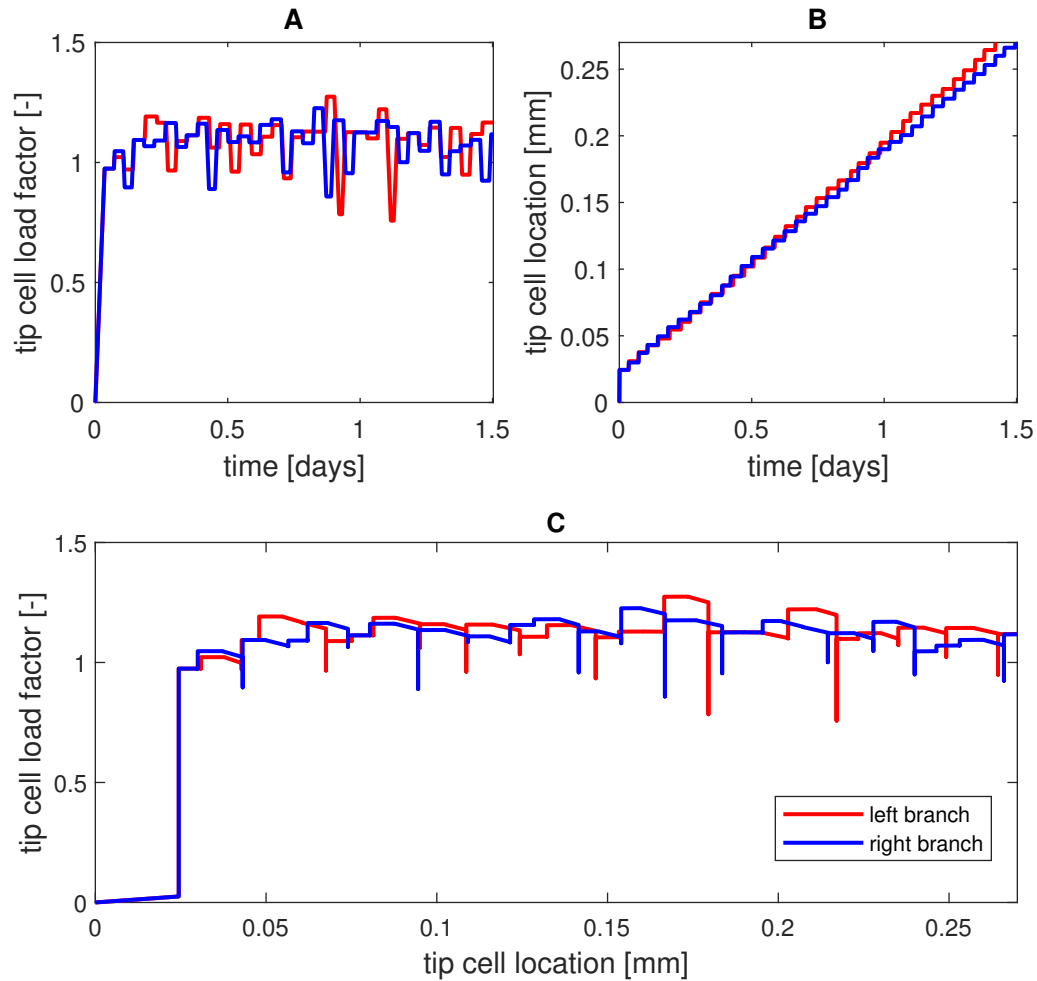
Figure 5.7: Tip cell load factor and tip cell location evolution throughout the analysis time for model III. The two plot colours stand for the two different branches shown in 5.6.

the first tip cell of the new branch will be in the normal direction of the current vessel. The first two assumptions are made so that the branching would not be affected by the transition diffusion depth, parameter l, of the other capillaries. Decreasing the element size and the length-scale parameter will ease the constraints.

Running the simulations with the above constraints results in Figure 5.8. The first
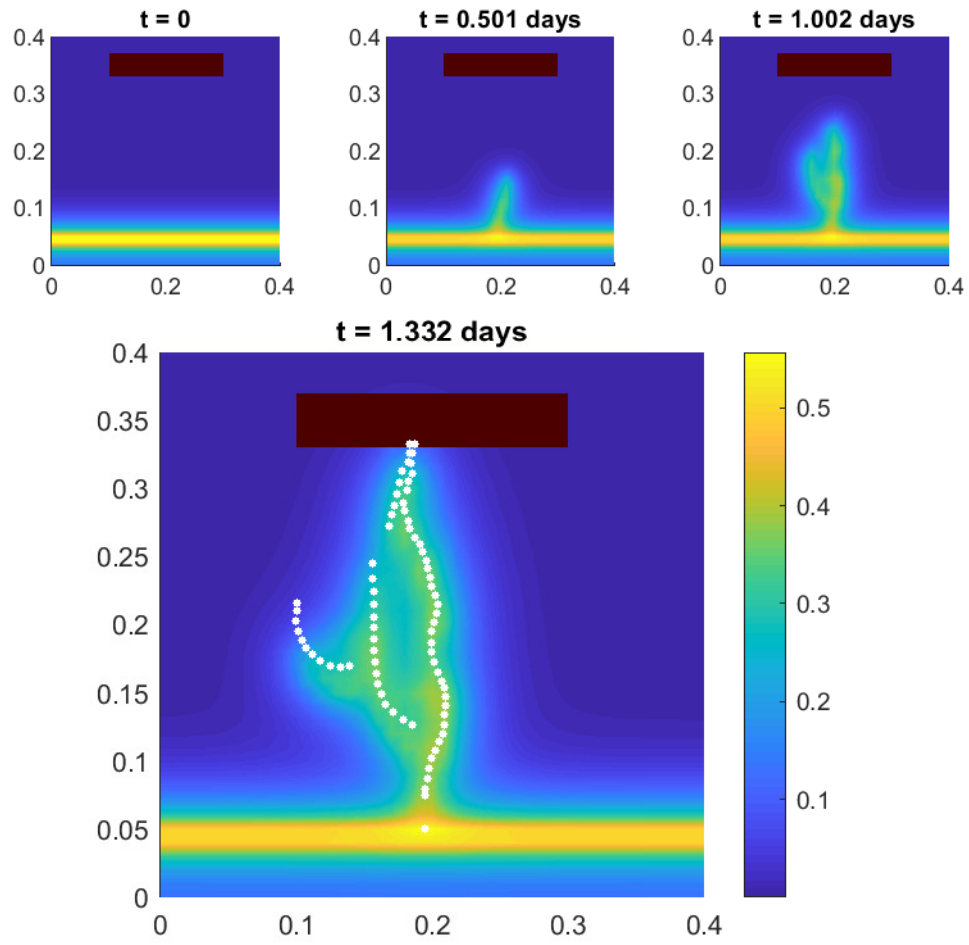
Figure 5.8: The growth of one capillary towards a tumour for model IV. This model is different from the second model by turning the branching engine on.

branch initiated at $t = 0.51$ days and followed by the second one at $t = 1.01$ days. As mentioned before, in this model the tip cells are closer to each other than as seen in model III. At the time that the first branching occurs, the distance between the two tip cells is
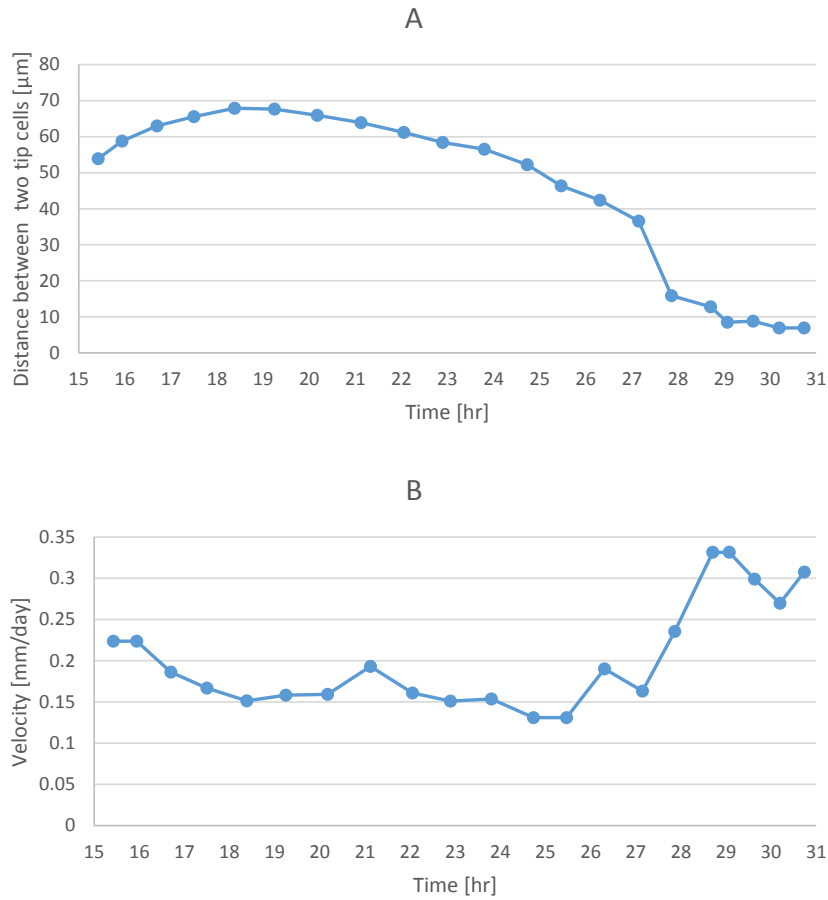
Figure 5.9: Relationship between the distance between the two tip cells right after the first branching occurs and the velocity of migration of the main branch.

53.9 μm. As shown in Figure 5.9A, this distance increases initially and then decreases but stays over the effective range, 54 μm, for the first 24.5 hours of the simulation. The decrease continues to the degree that at $t = 30.7$ h the distance between the two tip cells reaches 6.94 μm. The stress fields of the adjacent tip cells result in bigger local deformations and higher potential energy. This results in the energy-based crack criterion being met sooner

and finally in a faster migration towards the tumour. Figure 5.9B is the evidence for this increase in migration speed. This is the greatest significance of this modelling approach. It shows the role of the mechanical properties and the mechanical fields on the progress of angiogenesis.

5.5   Verification

Comprehensive verification of this model is a challenge because of the type of outputs produced by the model. These outputs include the displacement and stress fields in addition to the phase-change variable (*i.e.* changing of the ECM to the EC lining the blood vessels). Due to the difficulties associated with experimental measurement, little attention has been paid in literature to measure these parameters as extensive as shown here. Therefore, limited verification was conducted and focused on some defining outputs which are extracted and compared to available experimental data.

The two defining outputs are the width of the capillaries and speed of the endothelial cells migration. The newly-formed capillaries have the width of about 10 μm which is represented by the yellow zone in branches in figures such as in Figure 5.7. This width is close to the average capillary width [19] of around 9 μm. The measured speed of tip cells migration in the proposed model is about 7.5 μm/hr. This is acquired by determining the average speed of the endothelial cells migration throughout the entire time frame of the model which is close to 6.0 μm/hr proposed in [26] and is in the range suggested in the mathematical models by Zaman and DiMilla [87, 88] and the experimental data in [89].

Other characteristics like the direction of the endothelial cells movement and the occurrence of branching can be modified easily by changing their respected parameters in the vascular network module and are not discussed here.

5.6 Conclusion

This chapter started with acquiring most of the parameters' values from the literature and setting the rest by calibrating the model with respect to the results in the model proposed by McDougall [26]. Then, initial and boundary conditions were set, and a domain was defined to run the analysis. Four different simulations as shown by Table 5.4 were run, and the results were discussed. Each of the four simulations became more detailed and added new aspects of angiogenesis. The experimental observations verified the model by comparing the defining characteristics seen *in vitro* with the output of the *in silico* model. These defining characteristics are the vessel width and the migration speed of the tip cells and were found compatible with the experimental observations.

Overall, this chapter shows the stability of the model proposed here and the power it holds.

Chapter 6

Conclusion & Future Works

6.1 Conclusion

Some *in silico* tumour-induced angiogenesis models are proposed every year. Each of these models tries to focus and capture distinct aspects of the complex phenomenon [90, 91]. The core of the model developed in this research is the mechanical aspect of the propagation of the endothelial cells in the extracellular matrix. This work models the matrical pathways in angiogenesis with fracture mechanics formulation. This formation of matrix pathways in the ECM is assumed to be equivalent to the migration of the ECs. A modular solver with three modules is the backbone of this research with each module accounting for one aspect of the phenomenon. One of the novelties in this solver is the integration of ductile fracture mechanics in the phase-field equation. This innovation is based on the crack phase-field equations proposed in [92, 3]. Unlike the hybrid models in the literature, the continuum and discrete components here are more interrelated than the models which extract a velocity function from the continuum component for the movement of the tip cell. The solver

implements finite element method to solve the PDEs present in the continuum component.

Several numerical simulations presented here prove the stability and reliability of the framework. Yet, there is a need for a better calibration of the parameters given in tables 5.1, 5.2, and 5.3 with more experimental data. Also, further improvement of the model can result in a better understanding of the processes in tumour progression with a potential contribution to new treatments for cancer, as mentioned in the next section. The treatments in mind here are solid mechanics related. An example of this is increasing the energy needed for the fracture of the extracellular matrix or make it more resistant to the MDEs so that the ECM averts the progression of angiogenesis.

6.2   Future Works

The experimental data on angiogenesis is still minimal but yet, a lot of theoretical improvements can be added to the solver presented in this work to make the model more comprehensive and more realistic. The list of improvements is as follows:

- Branching and anastomosis are the first two essential phenomena that need to be improved in the modelling. Most of the algorithms found in the literature purely rely on experimental works with no good theories existing on these matters yet.

- Incorporating higher-order phase-field function [71] like the one discussed in 3.27; for numerical implementation there is need for using either higher-order finite element [93, 94], *i.e.* Hermite shape functions, or isogeometric analysis for providing $\mathcal{H}^2$ space using C^1 shape functions.

- Isogeometric Analysis [70, 95] is the only computational feasible way to produce C^1

shape functions in a three-dimensional space. It can help better integrate the geometry with no significant increase in computational cost. Incorporating isogeometric analysis in future modellings instead of conventional finite elements can facilitate the usage of higher-order phase-field functions.

- Better degradation functions for better modelling of the softening behaviour associated with the mechanical aspect of phase transition. Many experiments need to be performed to find the best degradation function such as the cubic degradation function as seen in 3.48 [81, 61].

- The cells life cycles can be modelled by modelling mitosis, apoptosis, and necrosis in the endothelial cells [48]. The last term in 3.77 is an example of the modelling of mitosis.

- More parameters can be used to construct multiphase-field model[96]. The phase-field parameter defined in this work showed the interface between the endothelial cells and the extracellular matrix. The new parameters can model other phases such as the lumen.

- Porous material properties for the ECM can be applied. Also, fluid mechanics and solid-fluid interaction can be added for modelling the blood flow using [92, 97].

- The force exerted on the matrix for the migration process needs some more extensive experimental work to develop better equations.

- Agent-based modelling can be introduced to model the discrete parts of the problem [64, 98] in the vascular network module.

- Cellular potts approach can be used instead of phase-field approach which integrates the cells individually [99].

References

[1] V. Vavourakis, P. Wijeratne, R. Shipley, M. Loizidou, T. Stylianopoulos, and D. Hawkes, "A validated multiscale in-silico model for mechano-sensitive tumour angiogenesis and growth," *PLoS Computational Biology*, vol. 13, no. 1, 2017, cited By 5. [Online]. Available: https://www.scopus.com/inward/record.uri?eid=2-s2.0-85011320212&doi=10.1371%2fjournal.pcbi.1005259&partnerID=40&md5=2e741a3dec7943d72c55d669a566773f

[2] M. C., W. F., and H. M., "Thermodynamically consistent phasefield models of fracture: Variational principles and multifield fe implementations," *International Journal for Numerical Methods in Engineering*, vol. 83, no. 10, pp. 1273–1311, 2010. [Online]. Available: https://onlinelibrary.wiley.com/doi/abs/10.1002/nme.2861

[3] O. Gultekin, H. Dal, and G. A. Holzapfel, "A phase-field approach to model fracture of arterial walls: Theory and finite element analysis," *Computer Methods in Applied Mechanics and Engineering*, vol. 312, pp. 542 – 566, 2016, phase Field Approaches to Fracture. [Online]. Available: http://www.sciencedirect.com/science/article/pii/S0045782516301645

[4] L. D. Black, P. G. Allen, S. M. Morris, P. J. Stone, and B. Suki, "Mechanical and failure properties of extracellular matrix sheets as a function of structural protein composition." *Biophysical journal*, vol. 94, no. 5, pp. 1916–1929, mar 2008.

[5] L. Edgar, S. Maas, J. Guilkey, and J. Weiss, "A coupled model of neovessel growth and matrix mechanics describes and predicts angiogenesis in vitro," *Biomechanics and Modeling in Mechanobiology*, vol. 14, no. 4, pp. 767–782, 2015, cited By 5. [Online]. Available: https://www.scopus.com/inward/record.uri?eid=2-s2.0-84939418025&doi=10.1007%2fs10237-014-0635-z&partnerID=40&md5=b478845d3f6f7b740618e539fb189cf2

[6] C. A. Reinhart-King, M. Dembo, and D. A. Hammer, "Cell-cell mechanical communication through compliant substrates," *Biophysical Journal*, vol. 95, no. 12, pp. 6044 – 6051, 2008. [Online]. Available: http://www.sciencedirect.com/science/article/pii/S0006349508820188

[7] ——, "The dynamics and mechanics of endothelial cell spreading," *Biophysical Journal*, vol. 89, no. 1, pp. 676 – 689, 2005. [Online]. Available: http://www.sciencedirect.com/science/article/pii/S0006349505727132

[8] Canadian Cancer Society's Advisory Committee on Cancer Statistics, "Canadian Cancer Statistics 2017," *Canadian Cancer Society*, pp. 1–132, 2017. [Online]. Available: http://www.cancer.ca/{~}/media/cancer.ca/CW/cancerinformation/cancer101/Canadiancancerstatistics/Canadian-Cancer-Statistics-2017-EN.pdf?la=en

[9] D. Hanahan and R. Weinberg, "The hallmarks of cancer," *Cell*, vol. 100, no. 1, pp. 57–70, 2000, cited By 17202. [Online]. Available: https://www.scopus.com/inward/

record.uri?eid=2-s2.0-0034614637&doi=10.1016%2fS0092-8674%2800%2981683-9&partnerID=40&md5=89bc353529ff03dcaef780b65a85b445

[10] D. Hanahan and R. A. Weinberg, "Hallmarks of cancer: the next generation," *cell*, vol. 144, no. 5, pp. 646–674, 2011.

[11] Dorland, *Dorland's Illustrated Medical Dictionary*, 32nd ed. Philadelphia, PA: Saunders/Elsevier, 2011.

[12] P. Lenzi, G. Bocci, and G. Natale, "John hunter and the origin of the term "angiogenesis"," *Angiogenesis*, vol. 19, no. 2, pp. 255–256, Apr 2016. [Online]. Available: https://doi.org/10.1007/s10456-016-9496-7

[13] L. Lamalice, F. Le Boeuf, and J. Huot, "Endothelial cell migration during angiogenesis," *Circulation Research*, vol. 100, no. 6, pp. 782–794, 2007. [Online]. Available: http://circres.ahajournals.org/content/100/6/782

[14] B. P. H., H. Ruslan, and D. Valentin, "Intussusceptive angiogenesis: Its emergence, its characteristics, and its significance," *Developmental Dynamics*, vol. 231, no. 3, pp. 474–488, 2004. [Online]. Available: https://onlinelibrary.wiley.com/doi/abs/10.1002/dvdy.20184

[15] T. H. Adair and J.-P. Montani, *Angiogenesis.* Morgan & Claypool Life Sciences, 2011.

[16] A. R. A. Anderson, M. A. J. Chaplain, and S. McDougall, *A Hybrid Discrete-Continuum Model of Tumour Induced Angiogenesis.* New York, NY: Springer New York, 2012, pp. 105–133. [Online]. Available: https://doi.org/10.1007/978-1-4614-0052-3_5

[17] A. B. Tepole, "Computational systems mechanobiology of wound healing," *Computer Methods in Applied Mechanics and Engineering*, vol. 314, pp. 46 – 70, 2017, special Issue on Biological Systems Dedicated to William S. Klug. [Online]. Available: http://www.sciencedirect.com/science/article/pii/S0045782516302857

[18] D. Ribatti and E. Crivellato, "sprouting angiogenesis, a reappraisal," *Developmental Biology*, vol. 372, no. 2, pp. 157 – 165, 2012. [Online]. Available: http://www.sciencedirect.com/science/article/pii/S0012160612005362

[19] Y.-T. Shiu, J. A. Weiss, J. B. Hoying, M. N. Iwamoto, I. S. Joung, and C. T. Quam, "The role of mechanical stresses in angiogenesis," *Critical Reviews in Biomedical Engineering*, vol. 33, no. 5, pp. 431–510, 2005. [Online]. Available: https://www.scopus.com/inward/record.uri?eid=2-s2.0-23944492296{/&}partnerID=40{/&}md5=a390df115b84f4dbeae983b9b3d39af3

[20] J. Kerr, A. Wyllie, and A. Currie, "Apoptosis: A basic biological phenomenon with wide-ranging implications in tissue kinetics," *British Journal of Cancer*, vol. 26, no. 4, pp. 239–257, 1972, cited By 11072. [Online]. Available: https://www.scopus.com/inward/record.uri?eid=2-s2.0-0015383455&doi=10.1038%2fbjc.1972.33&partnerID=40&md5=d965dc8d46728b26e9327cf8b19a01a9

[21] ""homeostasis"," *The Lancet*, vol. 225, no. 5817, pp. 445–446, 1935, cited By 0. [Online]. Available: https://www.scopus.com/inward/record.uri?eid=2-s2.0-50249196489&doi=10.1016%2fS0140-6736%2800%2957105-0&partnerID=40&md5=c1d6a21bf704a3140d7d1e045ae6aeb2

[22] M. Hejmadi, *Introduction to cancer biology*, 2nd ed. Ventus Publishing, 2010.

[23] C. Phipps, H. Molavian, and M. Kohandel, "A microscale mathematical model for metabolic symbiosis: Investigating the effects of metabolic inhibition on ATP turnover in tumors," *Journal of Theoretical Biology*, vol. 366, pp. 103–114, 2015. [Online]. Available: http://dx.doi.org/10.1016/j.jtbi.2014.11.016

[24] A. Malandrino, M. Mak, R. Kamm, and E. Moeendarbary, "Complex mechanics of the heterogeneous extracellular matrix in cancer," *Extreme Mechanics Letters*, vol. 21, pp. 25–34, 2018, cited By 0. [Online]. Available: https://www.scopus.com/inward/record.uri?eid=2-s2.0-85044535196&doi=10.1016%2fj.eml.2018.02.003&partnerID=40&md5=fc70d8baad45f24c17dd8da32d75e7ba

[25] J. Folkman, "Tumor angiogenesis: Therapeutic implications," *New England Journal of Medicine*, vol. 285, no. 21, pp. 1182–1186, 1971, pMID: 4938153. [Online]. Available: https://doi.org/10.1056/NEJM197111182852108

[26] S. McDougall, A. Anderson, and M. Chaplain, "Mathematical modelling of dynamic adaptive tumour-induced angiogenesis: Clinical implications and therapeutic targeting strategies," *Journal of Theoretical Biology*, vol. 241, no. 3, pp. 564–589, 2006, cited By 200. [Online]. Available: https://www.scopus.com/inward/record.uri?eid=2-s2.0-33745918670&doi=10.1016%2fj.jtbi.2005.12.022&partnerID=40&md5=7baef37b9da18dce293f1950328ce096

[27] A. Harris, "Hypoxia - a key regulatory factor in tumour growth," *Nature Reviews Cancer*, vol. 2, no. 1, pp. 38–47, 2002, cited By 3216. [Online]. Available: https://www.scopus.com/inward/record.uri?eid=2-s2.0-0036359548&partnerID=40&md5=5b49f8f5a788fc3cdd8b397c07f0aa2f

[28] N. Blumberg, "Tumor angiogenesis factor. speculations on an approach to cancer chemotherapy," *Yale Journal of Biology and Medicine*, vol. 47, no. 2, pp. 71–81, 1974, cited By 4. [Online]. Available: https://www.scopus.com/inward/record.uri?eid=2-s2.0-0016289525&partnerID=40&md5=78f133a984156ed867a7b38fd7d27a28

[29] N. Ferrara, H.-P. Gerber, and J. LeCouter, "The biology of vegf and its receptors," *Nature Medicine*, vol. 9, no. 6, pp. 669–676, 2003, cited By 6132. [Online]. Available: https://www.scopus.com/inward/record.uri?eid=2-s2.0-0037699954&doi=10.1038%2fnm0603-669&partnerID=40&md5=da153412c0a9a4aa7f0ba6584a5adc44

[30] A. Anderson and M. Chaplain, "Continuous and discrete mathematical models of tumor-induced angiogenesis," *Bulletin of Mathematical Biology*, vol. 60, no. 5, pp. 857–899, 1998, cited By 626.

[31] G. Wadhams and J. Armitage, "Making sense of it all: Bacterial chemotaxis," *Nature Reviews Molecular Cell Biology*, vol. 5, no. 12, pp. 1024–1037, 2004, cited By 627.

[32] P. Wolfgang, R. Madlen, S. Carsten, and S. Carmen, "Endogenous migration modulators as parent compounds for the development of novel cardiovascular and antiinflammatory drugs," *British Journal of Pharmacology*, vol. 165, no. 7, pp. 2044–2058, 2011. [Online]. Available: https://bpspubs.onlinelibrary.wiley.com/doi/abs/10.1111/j.1476-5381.2011.01762.x

[33] S. Carter, "Haptotaxis and the mechanism of cell motility," *Nature*, vol. 213, no. 5073, pp. 256–260, 1967, cited By 307. [Online]. Available: https://www.scopus.com/inward/record.uri?eid=2-s2.0-0014212671&doi=10.1038%2f213256a0&partnerID=40&md5=276bc3680854dbbddf929775a614212d

[34] M. Chaplain, "Mathematical modelling of angiogenesis," *Journal of Neuro-Oncology*, vol. 50, no. 1-2, pp. 37–51, 2000, cited By 90. [Online]. Available: https://www.scopus.com/inward/record.uri?eid=2-s2.0-0034470377&doi=10.1023%2fA%3a1006446020377&partnerID=40&md5=16f762bff567769a2f22100c13491d84

[35] H. Keller, J. Wissler, and J. Ploem, "Chemotaxis is not a special case of haptotaxis," *Experientia*, vol. 35, no. 12, pp. 1669–1671, 1979, cited By 5. [Online]. Available: https://www.scopus.com/inward/record.uri?eid=2-s2.0-0018618832&doi=10.1007%2fBF01953261&partnerID=40&md5=333012edb0c8bb9ed2a2d629df34bf94

[36] S. Ricoult, T. Kennedy, and D. Juncker, "Substrate-bound protein gradients to study haptotaxis," *Frontiers in Bioengineering and Biotechnology*, vol. 3, no. MAR, 2015, cited By 13. [Online]. Available: https://www.scopus.com/inward/record.uri?eid=2-s2.0-84969439934&doi=10.3389%2ffbioe.2015.00040&partnerID=40&md5=d8e29b99e5ffe9aecbefad8ac2f14a70

[37] H. Eilken and R. Adams, "Dynamics of endothelial cell behavior in sprouting angiogenesis," *Current Opinion in Cell Biology*, vol. 22, no. 5, pp. 617–625, 2010, cited By 232.

[38] P. Macklin, S. McDougall, A. R. A. Anderson, M. A. J. Chaplain, V. Cristini, and J. Lowengrub, "Multiscale modelling and nonlinear simulation of vascular tumour growth," *Journal of Mathematical Biology*, vol. 58, no. 4, pp. 765–798, Apr 2009. [Online]. Available: https://doi.org/10.1007/s00285-008-0216-9

[39] M. C. Kim, R. Abeyaratne, R. D. Kamm, and H. H. Asada, "Dynamic modeling of cancer cell migration in an extracellular matrix fiber network," in *2017 American Control Conference (ACC)*, May 2017, pp. 779–784.

[40] W. Stetler-Stevenson, "Matrix metalloproteinases in angiogenesis: A moving target for therapeutic intervention," *Journal of Clinical Investigation*, vol. 103, no. 9, pp. 1237–1241, 1999, cited By 612. [Online]. Available: https://www.scopus.com/inward/record.uri?eid=2-s2.0-0033134622&doi=10.1172%2fJCI6870&partnerID=40&md5=14fe9fe0cea560e25e6930d6864d3887

[41] R. B. Vernon and E. H. Sage, "Between molecules and morphology. extracellular matrix and creation of vascular form." *The American journal of pathology*, vol. 147, no. 4, p. 873, 1995.

[42] G. Vilanova, I. Colominas, and H. Gomez, "Computational modeling of tumor-induced angiogenesis," *Archives of Computational Methods in Engineering*, vol. 24, no. 4, pp. 1071–1102, 2017, cited By 0.

[43] D. Zawicki, R. Jain, G. Schmid-Schoenbein, and S. Chien, "Dynamics of neovascularization in normal tissue," *Microvascular Research*, vol. 21, no. 1, pp. 27–47, 1981, cited By 79.

[44] S. McDougall, A. Anderson, M. Chaplain, and J. Sherratt, "Mathematical modelling of flow through vascular networks: Implications for tumour-induced angiogenesis and chemotherapy strategies," *Bulletin of Mathematical Biology*, vol. 64, no. 4, pp. 673–702, 2002, cited By 206. [Online]. Available: https://www.scopus.com/inward/record.uri?eid=2-s2.0-0036664608&doi=10.1006%2fbulm.2002.0293&partnerID=40&md5=625bea9e46980d73d48353809805626e

[45] L. Lamalice, F. Le Boeuf, and J. Huot, "Endothelial cell migration during angiogenesis," *Circulation Research*, vol. 100, no. 6, pp. 782–794, 2007, cited By 618.

[46] J. D. Murray and G. F. Oster, "Cell traction models for generating pattern and form in morphogenesis," *Journal of Mathematical Biology*, vol. 19, no. 3, pp. 265–279, Jul 1984. [Online]. Available: https://doi.org/10.1007/BF00277099

[47] D. Manoussaki, S. R. Lubkin, R. B. Vemon, and J. D. Murray, "A mechanical model for the formation of vascular networks in vitro," *Acta Biotheoretica*, vol. 44, no. 3, pp. 271–282, Nov 1996. [Online]. Available: https://doi.org/10.1007/BF00046533

[48] M. Holmes and B. Sleeman, "A mathematical model of tumour angiogenesis incorporating cellular traction and viscoelastic effects," *Journal of Theoretical Biology*, vol. 202, no. 2, pp. 95–112, 2000, cited By 72.

[49] M. A. Meyers and K. K. Chawla, *Mechanical Behavior of Materials*, 2nd ed. Cambridge University Press, 2008.

[50] D. Manoussaki, "A mechanochemical model of angiogenesis and vasculogenesis," *Mathematical Modelling and Numerical Analysis*, vol. 37, no. 4, pp. 581–599, 2003, cited By 45.

[51] P. Santos-Oliveira, A. Correia, T. Rodrigues, T. Ribeiro-Rodrigues, P. Matafome, J. Rodrguez-Manzaneque, R. Seia, H. Giro, and R. Travasso, "The force at the tip - modelling tension and proliferation in sprouting angiogenesis," *PLoS Computational Biology*, vol. 11, no. 8, 2015, cited By 9. [Online]. Available: https://www.scopus.com/inward/record.uri?eid=2-s2.0-84940778593&doi=10.1371%2fjournal.pcbi.1004436&partnerID=40&md5=62bc6857029577831d39b3caf505b5b0

[52] B. S. Biner, *Programming Phase-Field Modeling*, 1st ed. Springer International Publishing, 2017.

[53] J. W. Cahn and J. E. Hilliard, "Free energy of a nonuniform system. i. interfacial free energy," *The Journal of Chemical Physics*, vol. 28, no. 2, pp. 258–267, 1958. [Online]. Available: https://doi.org/10.1063/1.1744102

[54] S. Allen and J. Cahn, "Ground state structures in ordered binary alloys with second neighbor interactions," *Acta Metallurgica*, vol. 20, no. 3, pp. 423 – 433, 1972. [Online]. Available: http://www.sciencedirect.com/science/article/pii/0001616072900375

[55] L.-Q. Chen and W. Yang, "Computer simulation of the domain dynamics of a quenched system with a large number of nonconserved order parameters: The grain-growth kinetics," *Phys. Rev. B*, vol. 50, pp. 15 752–15 756, Dec 1994. [Online]. Available: https://link.aps.org/doi/10.1103/PhysRevB.50.15752

[56] A. A. Griffith, "Vi. the phenomena of rupture and flow in solids," *Philosophical Transactions of the Royal Society of London A: Mathematical, Physical and Engineering Sciences*, vol. 221, no. 582-593, pp. 163–198, 1921. [Online]. Available: http://rsta.royalsocietypublishing.org/content/221/582-593/163

[57] F. Siegfried, *Handbuch der Physik: Encyclopedia of physics.* Springer., 1958.

[58] G. Francfort and J.-J. Marigo, "Revisiting brittle fracture as an energy minimization problem," *Journal of the Mechanics and Physics of Solids*, vol. 46, no. 8, pp. 1319 – 1342, 1998. [Online]. Available: http://www.sciencedirect.com/science/article/pii/S0022509698000349

[59] C. Miehe, M. Hofacker, and F. Welschinger, "A phase field model for rate-independent crack propagation: Robust algorithmic implementation based on operator splits," *Computer Methods in Applied Mechanics and Engineering*, vol. 199, no. 45, pp. 2765

– 2778, 2010. [Online]. Available: http://www.sciencedirect.com/science/article/pii/S0045782510001283

[60] A. Raina and C. Miehe, "A phase-field model for fracture in biological tissues," *Biomechanics and Modeling in Mechanobiology*, vol. 15, no. 3, pp. 479–496, Jun 2016. [Online]. Available: https://doi.org/10.1007/s10237-015-0702-0

[61] O. Gultekin, H. Dal, and G. A. Holzapfel, "Numerical aspects of anisotropic failure in soft biological tissues favor energy-based criteria: A rate-dependent anisotropic crack phase-field model," *Computer Methods in Applied Mechanics and Engineering*, vol. 331, pp. 23 – 52, 2018. [Online]. Available: http://www.sciencedirect.com/science/article/pii/S0045782517307132

[62] G. A. Holzapfel, T. C. Gasser, and R. W. Ogden, "A new constitutive framework for arterial wall mechanics and a comparative study of material models," *Journal of elasticity and the physical science of solids*, vol. 61, no. 1, pp. 1–48, Jul 2000. [Online]. Available: https://doi.org/10.1023/A:1010835316564

[63] T. C. Gasser, R. W. Ogden, and G. A. Holzapfel, "Hyperelastic modelling of arterial layers with distributed collagen fibre orientations," *Journal of The Royal Society Interface*, vol. 3, no. 6, pp. 15–35, 2006. [Online]. Available: http://rsif.royalsocietypublishing.org/content/3/6/15

[64] G. Vilanova, I. Colominas, and H. Gomez, "Capillary networks in tumor angiogenesis: From discrete endothelial cells to phase-field averaged descriptions via isogeometric analysis," *International journal for numerical methods in biomedical engineering*, vol. 29, no. 10, pp. 1015–1037, 2013.

[65] A. F. Bower, *Applied mechanics of solids.* CRC Press, 2010.

[66] R. W. Ogden, "Nonlinear continuum mechanics and modelling the elasticity of soft biological tissues with a focus on artery walls," in *Biomechanics: Trends in Modeling and Simulation*, ser. Studies in Mechanobiology, Tissue Engineering and Biomaterials, G. A. Holzapfel and R. W. Ogden, Eds.   Springer International Publishing, 2017, no. 20, pp. 83–156. [Online]. Available: http://eprints.gla.ac.uk/129548/

[67] M. Nicolas, D. John, and B. Ted, "A finite element method for crack growth without remeshing," *International Journal for Numerical Methods in Engineering*, vol. 46, no. 1, pp. 131–150, 1999. [Online]. Available: https://onlinelibrary.wiley.com/doi/abs/10.1002/%28SICI%291097-0207%2819990910%2946%3A1%3C131%3A%3AAID-NME726%3E3.0.CO%3B2-J

[68] N. Mos and T. Belytschko, "Extended finite element method for cohesive crack growth," *Engineering Fracture Mechanics*, vol. 69, no. 7, pp. 813 – 833, 2002. [Online]. Available: http://www.sciencedirect.com/science/article/pii/S001379440100128X

[69] A. Hansbo and P. Hansbo, "A finite element method for the simulation of strong and weak discontinuities in solid mechanics," *Computer Methods in Applied Mechanics and Engineering*, vol. 193, no. 33, pp. 3523 – 3540, 2004. [Online]. Available: http://www.sciencedirect.com/science/article/pii/S0045782504000507

[70] T. Hughes, J. Cottrell, and Y. Bazilevs, "Isogeometric analysis: Cad, finite elements, nurbs, exact geometry and mesh refinement," *Computer Methods in Applied Mechanics and Engineering*, vol. 194, no. 39, pp. 4135 – 4195, 2005. [Online]. Available: http://www.sciencedirect.com/science/article/pii/S0045782504005171

[71] M. J. Borden, T. J. Hughes, C. M. Landis, and C. V. Verhoosel, "A higher-order phase-field model for brittle fracture: Formulation and analysis

within the isogeometric analysis framework," *Computer Methods in Applied Mechanics and Engineering*, vol. 273, pp. 100 – 118, 2014. [Online]. Available: http://www.sciencedirect.com/science/article/pii/S0045782514000292

[72] H. Abe, K. Hayashi, and M. Sato, *Data Book on Mechanical Properties of Living Cells, Tissues, and Organs.* Springer Japan, 1996. [Online]. Available: https://books.google.ca/books?id=uYN0QgAACAAJ

[73] Y. Fung, *Biomechanics: Mechanical Properties of Living Tissues*, ser. Biomechanics. Springer New York, 1993. [Online]. Available: https://books.google.ca/books?id=4HaMStTGOHwC

[74] A. Schriefl, G. Zeindlinger, D. Pierce, P. Regitnig, and G. Holzapfel, "Determination of the layer-specific distributed collagen fibre orientations in human thoracic and abdominal aortas and common iliac arteries." *Journal of the Royal Society - Interface*, vol. 9, pp. 1275–1286, 2012.

[75] A. Al-Mayah, *Biomechanics of soft tissues: principles and applications.* CRC Press, an imprint of the Taylor & Francis Group, 2018.

[76] G. A. Holzapfel and R. W. Ogden, *Biomechanics of soft tissue in cardiovascular systems.* Springer, 2003.

[77] L. R. G. Treloar, "Stresses and birefringence in rubber subjected to general homogeneous strain," *Proceedings of the Physical Society*, vol. 60, no. 2, p. 135, 1948. [Online]. Available: http://stacks.iop.org/0959-5309/60/i=2/a=303

[78] R. Ogden, *Non-linear elastic deformations*, ser. Ellis Horwood series in mathematics and its applications. E. Horwood, 1984. [Online]. Available: https://books.google.ca/books?id=-pEeAQAAIAAJ

[79] L. T. Edgar, J. B. Hoying, and J. A. Weiss, "In silico investigation of angiogenesis with growth and stress generation coupled to local extracellular matrix density," *Annals of Biomedical Engineering*, vol. 43, no. 7, pp. 1531–1542, Jul 2015. [Online]. Available: https://doi.org/10.1007/s10439-015-1334-3

[80] W. J. Boettinger, J. A. Warren, C. Beckermann, and A. Karma, "Phase-field simulation of solidification," *Annual Review of Materials Research*, vol. 32, no. 1, pp. 163–194, 2002. [Online]. Available: https://doi.org/10.1146/annurev.matsci.32.101901.155803

[81] M. J. Borden, T. J. Hughes, C. M. Landis, A. Anvari, and I. J. Lee, "A phase-field formulation for fracture in ductile materials: Finite deformation balance law derivation, plastic degradation, and stress triaxiality effects," *Computer Methods in Applied Mechanics and Engineering*, vol. 312, pp. 130 – 166, 2016, phase Field Approaches to Fracture. [Online]. Available: http://www.sciencedirect.com/science/article/pii/S0045782516311069

[82] X. Zheng, S. M. Wise, and V. Cristini, "Nonlinear simulation of tumor necrosis, neo-vascularization and tissue invasion via an adaptive finite-element/level-set method," *Bulletin of Mathematical Biology*, vol. 67, no. 2, p. 211, Mar 2005. [Online]. Available: https://doi.org/10.1016/j.bulm.2004.08.001

[83] T. Bennett, *Transport by Advection and Diffusion*. Wiley Global Education, 2012. [Online]. Available: https://books.google.ca/books?id=wUscAAAAQBAJ

[84] B. Ingalls, *Mathematical Modeling in Systems Biology: An Introduction*, ser. MIT Press Series. MIT Press, 2013. [Online]. Available: https://books.google.ca/books?id=FR20AQAACAAJ

[85] J. Crank and P. Nicolson, "A practical method for numerical evaluation of solutions of partial differential equations of the heat-conduction type," *Advances in Computational Mathematics*, vol. 6, no. 1, pp. 207–226, Dec 1996. [Online]. Available: https://doi.org/10.1007/BF02127704

[86] R. S. Sopher, H. Tokash, S. Natan, M. Sharabi, O. Shelah, O. Tchaicheeyan, and A. Lesman, "Nonlinear elasticity of the extracellular matrix fibers facilitates efficient inter-cellular mechanical communication," *Biophysical Journal*, feb 2018. [Online]. Available: http://arxiv.org/abs/1802.05075

[87] M. H. Zaman, R. D. Kamm, P. Matsudaira, and D. A. Lauffenburger, "Computational model for cell migration in three-dimensional matrices," *Biophys. J.*, vol. 89, no. 2, pp. 1389–1397, Aug 2005.

[88] P. A. DiMilla, K. Barbee, and D. A. Lauffenburger, "Mathematical model for the effects of adhesion and mechanics on cell migration speed," *Biophys. J.*, vol. 60, no. 1, pp. 15–37, Jul 1991.

[89] S. P. Palecek, J. C. Loftus, M. H. Ginsberg, D. A. Lauffenburger, and A. F. Horwitz, "Integrin-ligand binding properties govern cell migration speed through cell-substratum adhesiveness," *Nature*, vol. 385, no. 6616, pp. 537–540, Feb 1997.

[90] S. Soleimani, M. Shamsi, M. Ghazani, H. Modarres, K. Valente, M. Saghafian, M. Ashani, M. Akbari, and A. Sanati-Nezhad, "Translational models of tumor angiogenesis: A nexus of in silico and in vitro models," *Biotechnology Advances*, vol. 36, no. 4, pp. 880–893, 2018, cited By 1. [Online]. Available: https://www.scopus.com/inward/record.uri?eid=2-s2.0-85042849993&doi=10.1016%2fj.biotechadv.2018.01.013&partnerID=40&md5=6944a795de039e15ce08e1c5b985d44c

[91] T. Heck, M. Vaeyens, and H. Van Oosterwyck, "Computational models of sprouting angiogenesis and cell migration: Towards multiscale mechanochemical models of angiogenesis," *Mathematical Modelling of Natural Phenomena*, vol. 10, no. 1, pp. 108–141, 2015, cited By 16. [Online]. Available: https://www.scopus.com/inward/record.uri?eid=2-s2.0-84922940990&doi=10.1051%2fmmnp%2f201510106&partnerID=40&md5=d426b0f7e3986e1926818e43ae9b8b32

[92] C. Miehe, S. Mauthe, and S. Teichtmeister, "Minimization principles for the coupled problem of darcybiot-type fluid transport in porous media linked to phase field modeling of fracture," *Journal of the Mechanics and Physics of Solids*, vol. 82, pp. 186 – 217, 2015. [Online]. Available: http://www.sciencedirect.com/science/article/pii/S0022509615000733

[93] J. N. Reddy, *An Introduction To The Finite Element Method*, ser. International student edition. Tmh, 1984. [Online]. Available: https://books.google.ca/books?id=DrsXnwEACAAJ

[94] G. Dhatt, E. Lefranois, and G. Touzot, *Finite Element Method*, ser. ISTE. Wiley, 2012. [Online]. Available: https://books.google.ca/books?id=wvE1ClcHq5IC

[95] J. A. Cottrell, T. J. R. Hughes, and Y. Bazilevs, *Isogeometric Analysis: Toward Integration of CAD and FEA*, 1st ed. Wiley Publishing, 2009.

[96] A. Donaldson, D. Kirpalani, and A. Macchi, "Diffuse interface tracking of immiscible fluids: Improving phase continuity through free energy density selection," *International Journal of Multiphase Flow*, vol. 37, no. 7, pp. 777 – 787, 2011. [Online]. Available: http://www.sciencedirect.com/science/article/pii/S0301932211000474

[97] S. Mauthe and C. Miehe, "Hydraulic fracture in poro-hydro-elastic media," *Mechanics Research Communications*, vol. 80, pp. 69 – 83, 2017, multi-Physics of Solids at Fracture. [Online]. Available: http://www.sciencedirect.com/science/article/pii/S0093641316301781

[98] Z. Wang, J. D. Butner, R. Kerketta, V. Cristini, and T. S. Deisboeck, "Simulating cancer growth with multiscale agent-based modeling," *Seminars in Cancer Biology*, vol. 30, pp. 70 – 78, 2015, cancer modeling and network biology. [Online]. Available: http://www.sciencedirect.com/science/article/pii/S1044579X14000492

[99] M. Scianna, L. Preziosi, and K. Wolf, "A cellular potts model simulating cell migration on and in matrix environments," *Mathematical Biosciences & Engineering*, vol. 10, pp. 235–261, 2013. [Online]. Available: http://aimsciences.org//article/id/f177885a-006a-4b14-ab37-8096a72c798d